2007-01-02

A Numerical Vortex Approach To Aerodynamic Modeling of SUAV/VTOL Aircraft

Douglas F. Hunsaker
Brigham Young University - Provo

A NUMERICAL VORTEX APPROACH TO AERODYNAMIC MODELING OF SUAV/VTOL AIRCRAFT

by

Douglas F. Hunsaker

A thesis submitted to the faculty of

Brigham Young University

in partial fulfillment of the requirements for the degree of

Master of Science

Department of Mechanical Engineering

Brigham Young University

April 2007

BRIGHAM YOUNG UNIVERSITY

GRADUATE COMMITTEE APPROVAL

of a thesis submitted by

Douglas F. Hunsaker

This thesis has been read by each member of the following graduate committee and by majority vote has been found to be satisfactory.

Date	Deryl O. Snyder, Chair
Date	Timothy W. McLain
Date	Jeffrey P. Bons

BRIGHAM YOUNG UNIVERSITY

As chair of the candidate's graduate committee, I have read the thesis of Douglas F. Hunsaker in its final form and have found that (1) its format, citations, and bibliographical style are consistent and acceptable and fulfill university and department style requirements; (2) its illustrative materials including figures, tables, and charts are in place; and (3) the final manuscript is satisfactory to the graduate committee and is ready for submission to the university library.

_____
Date

_____
Deryl O. Snyder
Chair, Graduate Committee

Accepted for the Department

_____
Matthew R. Jones
Graduate Coordinator

Accepted for the College

_____
Alan R. Parkinson
Dean, Ira A. Fulton College of
Engineering and Technology

ABSTRACT

A NUMERICAL VORTEX APPROACH TO AERODYNAMIC MODELING OF SUAV/VTOL AIRCRAFT

Douglas F. Hunsaker

Department of Mechanical Engineering

Master of Science

A combined wing and propeller model is presented as a low-cost approach to preliminary modeling of slipstream effects on a finite wing. The wing aerodynamic model employs a numerical lifting-line method utilizing the 3D vortex lifting law along with known 2D airfoil data to predict the lift distribution across a wing for a prescribed upstream flowfield. The propeller/slipstream model uses blade element theory combined with momentum conservation equations. This model is expected to be of significant importance in the design of tail-sitter vertical take-off and landing (VTOL) aircraft, where the propeller slipstream is the primary source of air flow past the wings in some flight conditions. The algorithm is presented, and results compared with published experimental data.

ACKNOWLEDGMENTS

I would like to thank Dr. Snyder for his wise mentoring, guidance, and friendship throughout the progression of this research. Additionally, I'd like to thank my family members who have supported and encouraged me. Lastly, I'd like to thank the giants on whose shoulders I have been allowed to stand and from whose research I have learned and benefited.

Table of Contents

List of Figures

Chapter 1

Introduction

This chapter introduces the concepts of the thesis by presenting a short background, stating the objective, summarizing related work, and discussing the relevant contributions of the work as a whole.

1.1 Background

Interest in man-portable small unmanned air vehicles (SUAVs) has heightened recently as miniaturized autopilot and sensor capabilities have improved and increasingly complex SUAV missions have been conceived. Typical fixed wing SUAV configurations are often limited in their practical application due to the requirement of large take-off and landing areas and/or specialized take-off and landing equipment. In addition, the capability to persistently sense an area via a "perch-and-stare" approach has long been desired. In this mission scenario, the SUAV would be required to fly to a remote location, land, collect sensor data for an extended period of time, then take off and return to a specified rendezvous point—all without human assistance. These drawbacks and desired capabilities, among others, have directed attention toward the development of vertical take-off and landing (VTOL) SUAVs, specifically tail-sitter designs.

The concept of a tail-sitter VTOL aircraft has been around for over half a century. The main attraction of such an aircraft is the ability to take off and land in a manner similar to a rotorcraft, yet transition to efficient horizontal flight, thus achieving higher flight speeds and longer endurance and range. Likely, the most famous of these aircraft are the Convair XFY-1 Pogo (see Fig. 1.1) and the Lockheed XFV-1, developed and tested in the 1950's. These planes quickly proved that the tail-

sitter concept was substantially flawed, at least for piloted aircraft. After a relatively short test period, this concept was all but abandoned, mainly due to difficulties associated with a piloted landing. One must realize that the pilot was essentially laying on his back with no real view of the ground while trying to descend onto a target. However, when dealing with unmanned air vehicles under autonomous control, this problem no longer exists, and the tail-sitter becomes, conceptually, a viable solution.

Figure 1.1: The Convair XFY-1 Pogo in hovering flight.

The development of such VTOL aircraft presents many challenges for SUAVs, including power, controls, and aerodynamic modeling. VTOL aircraft experience airflow situations very foreign to conventional aircraft. For example, propwash effects are of secondary importance and are often ignored in preliminary designs of conventional aircraft, but cannot be neglected in the development of VTOL aircraft. Specifically during take-off, hovering, and landing, propwash effects become dominant where freestream flow from the aircraft's forward velocity is almost negligible. Additionally, current design tools are almost exclusively based on purely inviscid flow assumptions, which are questionable for Reynolds numbers less than 800,000, and certainly inadequate for Reynolds numbers less than 200,000. Thus, it becomes necessary to address, at least at some level, viscous effects in the early development of any SUAV aircraft.

Commonly, computational fluid dynamics (CFD) and/or experimental trial and error are used as design tools for development of fixed-wing SUAVs. Although one cannot argue that some success has been achieved, the time required to obtain results from these methods is too great to efficiently be used during the initial design phase. Rather, these are viable analysis tools to be employed after a design has reached some level of maturity. A design tool that rapidly and correctly predicts geometry, propwash, and Reynolds number effects on aerodynamic forces and moments is desirable.

1.2 Objective

This research presents a candidate approach to rapid aerodynamic modeling based on a numerical lifting line algorithm. The original algorithm is extended to allow for viscous effects from the 2D section lift and drag behavior and the effects of non-uniform airflow over a wing (i.e. jet/propwash effects) to be taken into account. This approach, rooted in inviscid theory, accounts for the effects of viscosity on the lift, drag, and moment behavior via semi-empirical corrections to an otherwise potential flow solution. This approach also requires a model to estimate the flowfield of a propeller. The propeller model employs blade element theory coupled with momentum equations. The resulting flowfield is added to the freestream velocity to create the input flowfield for the aerodynamic model.

1.3 Related Work

Although the lifting line and blade element algorithms are not new, the combination of the two to account for propeller effects on a 3D wing is unique.

Panel methods have been effectively used for a number of years in the initial stages of aircraft design. Blade element theories [1] and helical vortex models [2] have been employed to model propeller-induced flowfields with impressive success. These propeller models have been linked with panel methods to predict the aerodynamic influence of a propeller on a wing [3, 4]. Although sound, these methods often require a great deal of computational resources.

An alternative to panel methods has been suggested by Phillips [5] which extends Prandtl's lifting line theory to wings with sweep and washout. Phillips showed that the algorithm matched the accuracy of CFD solutions while requiring only a fraction of the computational cost. However, this extension of the lifting line theory has never been used to predict the effects of propwash on a wing.

Stone [6] combined a blade element theory with a panel method in the development of a tail-sitter UAV. The model was then used to create an aerodynamic database from which the aerodynamic forces and moments could be found through interpolation for dynamic simulation. Although the accuracy of the model is not quantitatively discussed, the model has produced reasonable results which have facilitated the development of the UAV. McCormick [7] has also intensely studied VTOL aerodynamics and presents simplified models for aerodynamic forces and moments of an aircraft in hover mode. His research is often cited to understand the basic phenomena of V/STOL flight.

1.4 Contributions

BYU faculty and students have undertaken an effort to develop the analysis tools, control algorithms, and system design of a VTOL SUAV. This research supports the development of this aircraft and provides a sound aerodynamic modeling package for students to use in the development of other aircraft for years to come. The following summarizes the main contributions of the research. This research

- provides a validated aerodynamic modeling package that can be implemented in the design phases of a VTOL SUAV.
- offers alternate solution methods to the equations of the numerical lifting line algorithm which allows a solution above stall.
- demonstrates the feasibility of the integrated propeller and lifting line models for analyzing VTOL flight.
- provides an analysis tool available to other students for future aircraft design projects.

1.4.1 Resulting Publications

Hunsaker, D. Snyder, D.O., "A Lifting-Line Approach to Estimating Propeller / Wing Interactions," 24th Applied Aerodynamics Conference, San Francisco, CA, June 5-8 2006

Hunsaker, D., "A Numerical Blade Element Approach to Estimating Propeller Flowfields," 45th AIAA Aerospace Sciences Meeting and Exhibit, Reno, Nevada, Jan. 2007 (Accepted)

1.5 Thesis Overview

The numerical model presented in this research can be divided into two sub-models: 1) an aerodynamic model (lifting line model), and 2) a propeller model (blade element model). The aerodynamic model is presented first because it is the core of the computational effort of the models. The propeller model is simply a tool to calculate the flowfield used as the input to the aerodynamic model.

The thesis is divided into four main sections. Chapters 2 and 3 present the algorithms for the lifting line model and the blade element model respectively along with relevant assumptions. Chapter 4 presents the validation of each model as well as the validation of the combined models by comparing the numerical results with published data. Chapter 5 discusses the integration of the model into a 6 DOF simulator. Chapter 6 presents the conclusions of the total work.

Chapter 2

Numerical Lifting Line Model

A numerical method based on Prandtl's classical lifting line theory is presented as a low computational cost approach to modeling slipstream effects on a finite wing. This method uses a 3D vortex lifting law along with known 2D airfoil data to predict the lift distribution across a wing.

2.1 Nomenclature

A_i	area of wing section i
$\bar{c}_i$	characteristic chord length for wing section i
c_i	average chord length at wing section i
C_{Di}	section drag coefficient for wing section i
C_{Li}	section lift coefficient for wing section i
$C_{L\alpha i}$	section lift slope for wing section i
C_{Mi}	section moment coefficient for wing section i
$\mathbf{d\ell_i}$	directed differential vortex length vector at control point i
$\mathbf{dF_i}$	section aerodynamic force vector for wing section i
dF_i	magnitude of $\mathbf{dF_i}$
f	system of equations
$\mathbf{F}$	total force on aircraft
$[\mathbf{J}]$	Jacobian matrix
$\mathbf{M}$	total moment on aircraft
N	total number of horseshoe vortices
$\mathbf{R}$	residual vector
R	magnitude of $\mathbf{R}$

$\mathbf{r_i}$	vector from aircraft CG to control point i
$\mathbf{r_{i_1j}}$	vector from 1^{st} node on section i to control point on section j
$\mathbf{r_{i_2j}}$	vector from 2^{nd} node on section i to control point on section j
r_{i_1j}	magnitude of $\mathbf{r_{i_1j}}$
r_{i_2j}	magnitude of $\mathbf{r_{i_2j}}$
S_i	planform area of wing section i
$\mathbf{u_{ai}}$	chordwise unit vector at control point i
$\mathbf{u_{ni}}$	normal unit vector at control point i
$\mathbf{u_{si}}$	spanwise unit vector at control point i
$\mathbf{u_i}$	unit vector in the direction of the local velocity
$\mathbf{v_{ij}}$	velocity induced at control point j by horseshoe vortex i
$\mathbf{V_i}$	velocity vector at control point i
V_i	magnitude of $\mathbf{V_i}$
V_{ai}	axial component of the velocity at control point i
V_{ni}	normal component of the velocity at control point i
$\mathbf{V_{rel_i}}$	upstream velocity at control point i
$\mathbf{V_{tot_i}}$	total velocity at control point i
V_{tot_i}	magnitude of $\mathbf{V_{tot_i}}$
α_i	angle of attack at wing section i
α_{L0i}	zero-lift angle of attack for with section i
δ_i	flap deflection for wing section i
$\delta\mathbf{M_i}$	section quarter-chord moment coefficient at wing section i
$\delta\mathbf{M}_{visc_i}$	viscous correction to the moment coefficient for wing section i
ϵ_i	flap efficiency for wing section i
$\mathbf{\Gamma}$	vector of vortex strengths
Γ_i	vortex strength at control point i
Ω	relaxation factor
ρ	fluid density

2.2 History

In the early 1900s, Ludwig Prandtl theorized that the lift caused by a three dimensional wing could be modeled by placing horseshoe-shaped vortices across the wing attached along the quarter chord as shown in Fig. 2.1. Each of these vortices would vary in magnitude, which would be at a maximum value in the center of the wing and taper out to zero at the wing tips where lift is virtually zero.

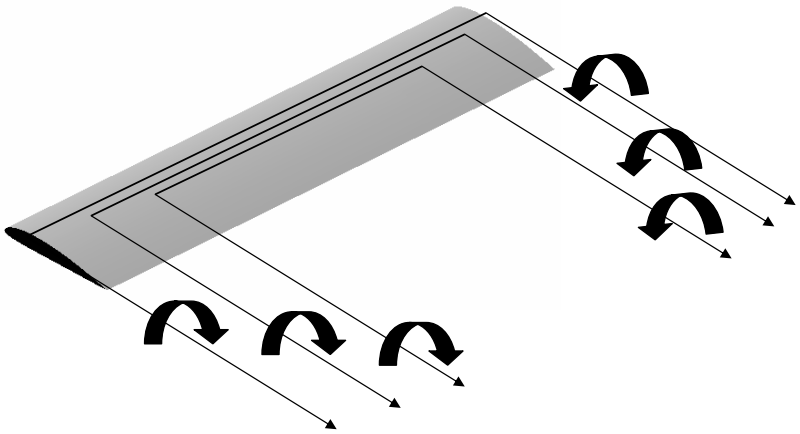

Figure 2.1: Prandtl's lifting line horseshoe-shaped vortex placement.

The magnitudes of each vortex could be directly translated to lift by the following vortex rule:

$$\mathbf{L} = \rho \mathbf{V}_\infty \Gamma \tag{2.1}$$

This equation shows that the lift at any wing section ($\mathbf{L}$) is equal to the air density (ρ) times the airstream velocity ($\mathbf{V}_\infty$) times the strength of the vortex at the wing section (Γ). If these horseshoe vortices were placed next to each other along the quarter-chord of the wing, the values for lift at each wing section could then be summed to calculate the total lift across a straight 3D wing. An explanation of the original lifting line theory can be found in almost any aerodynamics book. The reader is referred to Anderson [8] for a more thorough explanation.

This method for calculating the forces on a 3D wing has been widely used for many years due to the simplistic nature of the mathematics. After the development of the computer, other computational methods became popular and are still avidly used today. Recently, Phillips expanded the basic lifting line algorithm [5], suggesting that special placement of the vortices would allow the theory to account for sweep, taper, and washout of a 3D wing. Phillips's vortex placement can be seen in Fig. 2.2. This broadened the algorithm and made it capable of analyzing practical wing shapes. Along with this development, Phillips presented a method which allowed for a system of equations to be written and solved for a wing cut into a number of wing sections each having only one unknown: its local vortex magnitude. This system could then be solved for various aircraft configurations. The system of equations is nonlinear, requiring an iterative solver to converge within certain error criterion to the solution. Once the vortex magnitude at each wing section is known, it is converted to lift through the above equation and the results are summed to find the total lifting force over a wing.

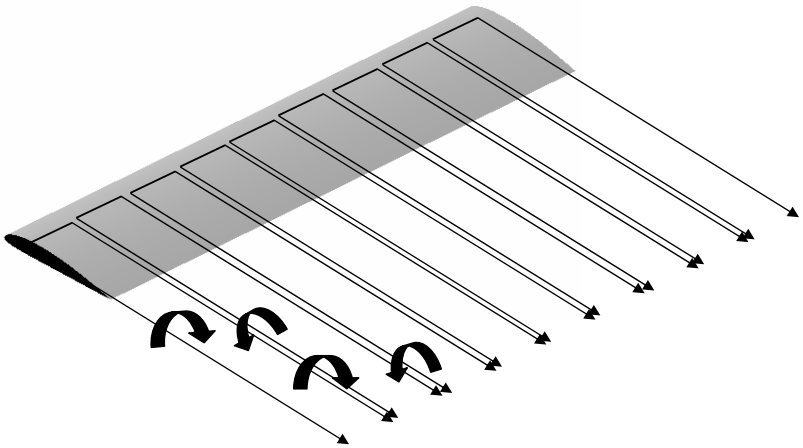

Figure 2.2: Phillips's lifting line horseshoe-shaped vortex placement.

2.3 Assumptions

2.3.1 Potential Flow

The original lifting line theory assumes potential flow. Such an assumption is quite valid at high Reynolds numbers and at low angles of attack. However, at angles of attack near or above stall, potential flow can no longer be assumed and corrections must be made. The approach presented here, although rooted in inviscid theory, accounts for the effects of viscosity on lift, drag, and moment via semi-empirical corrections to an otherwise potential flow solution. The viscous corrections are made by using 2D viscous data for the section lift and drag behavior. However, no attempt is made to correct the potential flow effects around the tips of wings. This means that although a wing may be separated from another lifting surface by only an extremely small distance, the lift at that wing tip could drop to zero. This is not physically true. In real life, viscous effects would prohibit the lift from dropping to zero at small gaps between wings.

2.3.2 2D Airfoil Characteristics At Each Spanwise Wing Section

The lifting line theory assumes that the lift generated at each spanwise location along the wing is equal to that of a 2D airfoil at the same effective angle of attack. (The effective angle of attack is the sum of the incident angle of attack to the freestream velocity and the induced angle of attack resulting from the downwash caused by the trailing vortices.) This assumption is in order for wings below stall and lends to very accurate results. It has been shown [9] that flows over wings at high angles of attack (i.e. above stall) have significant three dimensional properties. More specifically, at high angles of attack, the flow separates on the upper surface of the wing and a spanwise vortex forms along the wing. Thus, in order to accurately model the aerodynamics of a wing above stall, three dimensional effects should be taken into account. Although the lifting line theory assumes nearly two dimensional flow over each spanwise section of the wing, if post-stall data for the 2D airfoil is known, the assumption that the lift generated at each spanwise location is equal to that of a

2D airfoil at the same angle of attack should still be valid. This approach has been shown [10] to prove useful as a rough estimate to calculate wing lift above stall.

2.3.3 Elliptical Lift Distribution Initial Guess

High aspect ratio wings below stall have spanwise lift distributions which are very nearly elliptical in nature. Thus, for wings below stall, it is helpful to start with an initial elliptical circulation distribution. The formulation of such an initial guess is discussed in 2.5.1. This initial guess is also applied above stall, although it is not assumed that the final lift distribution will resemble an elliptical distribution. Thus it is assumed that an initial guess of an elliptical lift distribution produces reasonable results below and above stall.

2.4 Formulation

2.4.1 Overview

In the numerical lifting line method presented by Phillips [5], a finite wing is modeled using a series of horseshoe vortices with one edge bound to the quarter chord of the wing and the trailing portion aligned with the freestream velocity. A general 3D vortex lifting law is combined with Prandtl's hypothesis that each spanwise section of the wing has a section lift equivalent to that acting on a similar 2D airfoil with the same local angle of attack.

From the 3D vortex lifting law, the differential force vector produced by the finite wing section i is

$$\mathbf{dF_i} = \rho \Gamma_i \mathbf{V_i} \times \mathbf{d\ell_i} \tag{2.2}$$

The lift coefficient of a 2D airfoil can be expressed as an arbitrary function of angle of attack and flap deflection

$$C_{L_i} = C_{L_i}(\alpha_i, \delta_i) \tag{2.3}$$

Assuming that this relationship is known at each section, the magnitude of the differential force produced by wing section i is

$$dF_i = \frac{1}{2}\rho V_i^2 C_{L_i}(\alpha_i, \delta_i) A_i \tag{2.4}$$

Setting the magnitude of Eq. (2.2) equal to the right hand side of Eq. (2.4) for each of the spanwise sections of the wing produces a system of equations that can be solved for the vortex strengths at each section. Once all the vortex strengths are known, the force vector at each section can be computed and summed together to determine the force and moment vectors acting on the wing. This method has been shown to work well at predicting the inviscid forces and moments for wings with sweep and dihedral and aspect ratios greater than four. Accuracy is similar to panel methods or Euler computational fluid dynamics, but at a fraction of the cost. In addition, systems of lifting surfaces with arbitrary position and orientation can be analyzed.

2.4.2 Vortex Strengths

Typically, the numerical lifting line algorithm is developed in a nondimensional form. This is appropriate for conventional aircraft where the freestream velocity is used as a parameter for nondimensionalization. However, for VTOL flight analysis, where the freestream velocity can approach zero, a dimensional approach is better suited.

We begin by setting the magnitude of the force obtained from the section lift coefficient at wing section i, Eq. (2.4), equal to the magnitude of the forces determined from the 3D vortex lifting law, Eq. (2.2). After some rearrangement, we obtain

$$2\Gamma_i \left| \left(\mathbf{V_{rel_i}} + \sum_{j=1}^{N} \Gamma_j \mathbf{v_{ji}} \right) \times \mathbf{d\ell_i} \right| - V_{tot_i}^2 A_i C_{Li}(\alpha_i, \delta_i) = 0 \tag{2.5}$$

Note that on the LHS, the velocity of section i is split into the local upstream velocity $\mathbf{V_{rel_i}}$ and the velocity induced by all horseshoe vortices in the system (initially of unknown strength). The local upstream velocity differs from the global freestream

velocity in that it may also have contributions from prop-wash or rotations of the lifting surface about the aircraft center of gravity. The magnitude of the total velocity at wing section i is denoted as

$$V_{tot_i} = |\mathbf{V_{tot_i}}| = \left| \left(\mathbf{V_{rel_i}} + \sum_{j=1}^{N} \Gamma_j \mathbf{v_{ji}} \right) \right| \tag{2.6}$$

In the above expressions, $\mathbf{v_{ji}}$ is the normalized velocity induced at section i by horseshoe vortex j, calculated as

$$\mathbf{v_{ij}} = \frac{1}{4\pi} \left[\delta_{ij} \frac{(r_{i_1 j} + r_{i_2 j})(\mathbf{r_{i_1 j}} \times \mathbf{r_{i_2 j}})}{r_{i_1 j} r_{i_2 j} (r_{i_1 j} r_{i_2 j} + \mathbf{r_{i_1 j}} \cdot \mathbf{r_{i_2 j}})} \right] + \frac{1}{4\pi} \left[\frac{\mathbf{u_\infty} \times \mathbf{r_{i_2 j}}}{r_{i_2 j}(r_{i_2 j} - \mathbf{u_\infty} \cdot \mathbf{r_{i_2 j}})} - \frac{\mathbf{u_\infty} \times \mathbf{r_{i_1 j}}}{r_{i_1 j}(r_{i_1 j} - \mathbf{u_\infty} \cdot \mathbf{r_{i_1 j}})} \right] \tag{2.7}$$

where δ_{ij} is the Kronecker delta (1 if $i = j$, 0 if $i \neq j$). The local angle of attack at each section is calculated from the total velocity vector as

$$\alpha_i = \tan^{-1} \left[\frac{\left(\mathbf{V_{rel_i}} + \sum_{j=1}^{N} \Gamma_j \mathbf{v_{ji}} \right) \cdot \mathbf{u_{ni}}}{\left(\mathbf{V_{rel_i}} + \sum_{j=1}^{N} \Gamma_j \mathbf{v_{ji}} \right) \cdot \mathbf{u_{ai}}} \right] \tag{2.8}$$

Equation (2.5) defines a system of equations that can be solved for the unknown horseshoe vortex strengths Γ_i. The system can be written in the vector form

$$f(\mathbf{\Gamma}) = \mathbf{R} \tag{2.9}$$

where

$$f_i(\mathbf{\Gamma}) = 2\Gamma_i \left| \left(\mathbf{V_{rel_i}} + \sum_{j=1}^{N} \Gamma_j \mathbf{v_{ji}} \right) \times \mathbf{d\ell_i} \right| - V_{tot_i}^2 A_i C_{Li}(\alpha_i, \delta_i) \tag{2.10}$$

We seek the vector of horseshoe vortex strengths $\mathbf{\Gamma}$ that forces the residual vector $\mathbf{R}$ to zero. Notice that $\mathbf{V_{tot_i}}$ and α in Eq. (2.9) are both functions of Γ. Thus the system of equations is nonlinear and requires an iterative solver to converge on the solution.

2.4.3 Aerodynamic Forces and Moments

Once the magnitude of Γ_i at each wing section has been found, the forces resulting from the vortex strengths can be summed to find the overall aerodynamic force and moment acting on the aircraft. The total force on the aircraft is found by summing Eq. (2.2) over all wing sections:

$$\mathbf{F} = \rho \sum_{i=1}^{N} \left[\Gamma_i \left(\mathbf{V_{rel_i}} + \sum_{j=1}^{N} \Gamma_j \mathbf{v_{ji}} \right) \times \mathbf{d}\ell_\mathbf{i} \right] \tag{2.11}$$

Equation (2.11) provides the total inviscid force vector acting on the aircraft, and can be divided into the typical lift and induced drag components. A correction for the viscous drag [11] is added to the model based on the 2D airfoil drag behavior as a function of angle of attack:

$$\delta\mathbf{F}_{visc} = \sum_{i=1}^{N} \frac{1}{2} \rho V_{tot_i}^2 S_i C_{Di} \mathbf{u_i} \tag{2.12}$$

where C_{D_i} is the local 2D section drag coefficient (evaluated at the local angle of attack).

Similarly, the overall moment vector acting on the aircraft can be found from

$$\mathbf{M} = \rho \sum_{i=1}^{N} \mathbf{r_i} \times \left[\Gamma_i \left(\mathbf{V_{rel_i}} + \sum_{j=1}^{N} \Gamma_j \mathbf{v_{ji}} \right) \times \mathbf{d}\ell_\mathbf{i} \right] + \delta\mathbf{M_i} \tag{2.13}$$

where the first term is the moment due to the aerodynamic forces at each section acting at a moment arm about the center of gravity, and the second term $\delta\mathbf{M_i}$ is the 2D quarter-chord moment generated by each spanwise segment. $\delta\mathbf{M_i}$ can be easily obtained by assuming a constant moment coefficient over each wing section:

$$\delta\mathbf{M_i} = -\frac{1}{2} \rho V_{tot_i}^2 C_{Mi} \int_{s0}^{s1} c^2 \, ds \, \mathbf{u_{si}} \tag{2.14}$$

where $\mathbf{u_{si}}$ is the local spanwise unit vector.

A viscous correction [11] is also added to the overall moment vector to take into account the additional moment caused by the viscous drag force at each spanwise wing section:

$$\delta\mathbf{M}_{visc_i} = \sum_{i=1}^{N} \frac{1}{2}\rho V_{tot_i}^2 S_i C_{Di}(\mathbf{r_i} \times \mathbf{u_i}) \tag{2.15}$$

2.5 Solvers

The nonlinear system of equations has been solved using various techniques. Phillips [5] uses a Newton iteration method by calculating the Jacobian of the nondimensionalized system, while Anderson [10] uses a Picard iteration. Below stall the system displays different characteristics than above stall. A number of solvers were written in order to facilitate solving the nonlinear equations in both pre- and post-stall scenarios. Each of these solvers is described below.

2.5.1 Linearized System

In order to achieve the convergence criteria with a small number of iterations, it is important to obtain a good initial guess for $\mathbf{\Gamma}$. To do this, Phillips [5] suggests finding first a linearized approximation. This system is constructed from the original system of equations, Eq. (2.10), by dropping all second order terms and assuming a small induced angle of attack. The full derivation can be found in A.4. This results in the linear system

$$\frac{2\Gamma_i}{A_i C_{L\alpha i}} |\mathbf{V_{rel_i}} \times \mathbf{d\ell_i}| - V_{rel_i}^2 \left(\sum_{j=1}^{N} \frac{\Gamma_j \mathbf{v_{ji}} \cdot \mathbf{u_{ni}}}{V_{rel_j}} \right) = V_{rel_i}^2 \left(\tan^{-1} \left[\frac{\mathbf{V_{rel_i}} \cdot \mathbf{u_{ni}}}{\mathbf{V_{rel_i}} \cdot \mathbf{u_{ai}}} \right] - \alpha_{L0i} + \epsilon_i \delta_i \right) \tag{2.16}$$

Once this system is solved for the Γ_is, they can be used as the initial guess for other solvers.

2.5.2 Adjusted Linear Solver

A careful look at the linear solver just described reveals that the resulting circulation distribution is always elliptical and directly proportional to the lift slope of the 2D airfoil. At high angles of attack, where the lift slope decreases and deviates from the initial lift slope of the airfoil, the linear method produces results with significant over-predictions for the magnitudes of circulation. However, for most of the subsequent solvers to converge to a suitable answer, it was found necessary to start with an initial guess which was much closer to the expected final answer than the original linearization allowed. Thus it became necessary to find a way to "scale" the linear solution, especially above stall.

Two options for scaling the solution are presented here.

- Residual Scaling: From each solution, a residual can be calculated using Eq. (2.9) and Eq. (2.10). Scaling the circulation values by a factor likewise scales the residual. By applying a Jacobian-type solver to this scenario, the scaling factor can be found which minimizes the residual of the linear system solution.

- Solution Confidence Scaling: Once a solution has been calculated, one may note that there are two ways to calculate the resulting forces on the wing. The most common method is a result of the left half of Eq. (2.5), which is derived from Eq. (2.2). However, it is often helpful to approach the force calculations by using the right half of Eq. (2.5), which is derived from Eq. (2.4). Each of these equations can be used to calculate the total lift on the wing. If these two values for lift match perfectly, the circulation distribution solution can be trusted. Further, a significant difference between the two lift magnitudes would suggest that the solution is not sound. A "solution confidence" value can be calculated by taking the ratio of the smaller calculated lift to the larger. As this value approaches 1, the solution becomes increasingly valid. Scaling the circulation values by a factor affects the solution confidence value. By applying a Jacobian-type solver to this scenario, the scaling factor can be found which produces the solution with the highest solution confidence.

Note that the solutions resulting from either scaling method are still elliptical (for wings without propwash effects) and are simply scaled. The tests performed during this research suggest that the first method, residual scaling, produced the most valuable initial guesses for the subsequent solvers. This method is implemented in the resulting computer program. It is worth noting that both methods produced "better" initial guesses than not scaling the linear solution at all. Additionally, this scaled linear method has been found to be useful as a final solution estimate above stall when using another solver causes divergence or requires too much computational power.

2.5.3 Jacobian Solver

A reliable method for solving the nonlinear system below stall is by using Newton iterations. Simply stated, the vector of horseshoe vortex strengths $\mathbf{\Gamma}$ that forces the residual vector $\mathbf{R}$ to zero of Eq. (2.9) is needed. Starting with an initial guess for $\mathbf{\Gamma}$, we can compute the iterative change from

$$[\mathbf{J}]\mathbf{\Delta\Gamma} = -\mathbf{R} \tag{2.17}$$

where $[\mathbf{J}]$ is the N by N Jacobian matrix:

$$J_{ij} = \frac{\partial f_i}{\partial \Gamma_j} \tag{2.18}$$

This $\mathbf{\Delta\Gamma}$ is applied to the previous estimate of $\mathbf{\Gamma}$ and iterations are continued until convergence criterion are met.

Evaluating the partial derivatives of Eq. (2.10), we obtain

$$\begin{aligned} J_{ij} = \delta_{ij} 2|\mathbf{W_i}| + \frac{2\mathbf{W_i}\cdot(\mathbf{v_{ji}}\times\mathbf{d\ell_i})}{|\mathbf{W_i}|}\Gamma_i \\ - V_{tot_i}^2 A_i \frac{\partial C_{Li}}{\partial \alpha_i}\frac{V_{ai}(\mathbf{v_{ji}}\cdot\mathbf{u_{ni}}) - V_{ni}(\mathbf{v_{ji}}\cdot\mathbf{u_{ai}})}{V_{ai}^2 + V_{ni}^2} \\ - 2A_i C_{Li}(\alpha_i,\delta_i)(\mathbf{V_{tot}}\cdot\mathbf{v_{ji}}) \end{aligned} \tag{2.19}$$

where δ_{ij} is the Kronecker delta, and

$$\mathbf{W_i} = \left(\mathbf{V_{rel_i}} + \sum_{j=1}^{N} \Gamma_j \mathbf{v_{ji}} \right) \times \mathbf{d}\ell_\mathbf{i} \tag{2.20}$$

In Eq. (2.19) V_{ai} and V_{ni} are the axial and normal components of the local velocity, respectively:

$$V_{ai} = \left(\mathbf{V_{rel_i}} + \sum_{j=1}^{N} \Gamma_j \mathbf{v_{ji}} \right) \cdot \mathbf{u_{ai}} \tag{2.21}$$

$$V_{ni} = \left(\mathbf{V_{rel_i}} + \sum_{j=1}^{N} \Gamma_j \mathbf{v_{ji}} \right) \cdot \mathbf{u_{ni}} \tag{2.22}$$

where $\mathbf{u_{ai}}$ is the unit vector in the axial (chordwise) direction of section i, and $\mathbf{u_{ni}}$ is the unit vector in the normal direction of section i. The complete derivation of Eq. (2.19) can be found in A.3. When airfoil sections experience angles of attack beyond stall, the small or negative lift slope of the 2D airfoil data causes divergence of the Newton iterations. Thus it becomes necessary to explore other solvers.

2.5.4 Picard Solver

A common, simplistic approach to solving the nonlinear system of equations is through the use of Picard iterations. This solver begins with an initial guess (calculated from the Best Linear Solver explained above). The initial guess for the solution vector is used for any imbedded Γ vector within the system of equations that makes the system nonlinear. If these imbedded values for Γ are known, the system becomes a linear system and can be directly solved using an LU Decomposition routine. This produces a new solution vector which is theoretically closer to the real solution than the previous vector. This new guess is then used for the embedded vectors and the process is repeated until convergence criteria are met.

If Γ_{old} is known, the linear system can be written as

$$f_i(\mathbf{\Gamma}) = 2\Gamma_i \left| \left(\mathbf{V_{rel_i}} + \sum_{j=1}^{N} \Gamma_{j_{old}} \mathbf{v_{ji}} \right) \times \mathbf{d}\ell_\mathbf{i} \right| - V_{tot_i}^2 A_i C_{Li}(\alpha_i, \delta_i) \tag{2.23}$$

where Γ_{old} is used to calculate both V_{tot_i} and α. This system can be under-relaxed to minimize the probability of overstepping the solution.

$$\Gamma_{i_{new}} = \Omega \left(\Gamma_i - \Gamma_{i_{old}} \right) \tag{2.24}$$

The Picard Solver often requires more iterations to converge than the Jacobian Solver, but is able to find solutions above stall when the lift slope is negative.

2.5.5 Steepest Descent Solver

The idea behind a Steepest Descent Solver is also simplistic in nature, but requires a great deal more computational power than the Picard Solver. Starting from an initial guess, the gradient is found and a line search is performed in that direction until a local minimum is found. The local minimum is used as the new initial guess, and the process is repeated until convergence criteria are met.

The purpose of any of the solvers is to minimize the magnitude of the residual vector $\mathbf{R}$. We will call this magnitude R. We first seek the gradient of R where

$$R = \|\mathbf{R}\| = \|f(\mathbf{\Gamma})\| \tag{2.25}$$

This gradient can be found by applying small perturbations to the current solution and calculating the change in the residual with each perturbation. However, this is computationally expensive. Thus we seek a computationally efficient method for calculating $\nabla \|f(\mathbf{\Gamma})\|$. By setting

$$\|f(\mathbf{\Gamma})\| = \sqrt{(f(\mathbf{\Gamma})^2} \tag{2.26}$$

and

$$P(\mathbf{\Gamma}) = \frac{1}{2} \left(f_1(\mathbf{\Gamma})^2 + f_2(\mathbf{\Gamma})^2 + \ldots + (f_N(\mathbf{\Gamma})^2 \right) \tag{2.27}$$

it can be said that

$$\|f(\mathbf{\Gamma})\| \propto P(\mathbf{\Gamma}) \tag{2.28}$$

Therefore,

$$\nabla \|f(\mathbf{\Gamma})\| \propto \nabla P(\mathbf{\Gamma}) \tag{2.29}$$

where

$$\nabla P(\mathbf{\Gamma}) = \begin{bmatrix} f_1 \frac{\partial f_1}{\partial \Gamma_1} & + & \dots & + & f_N \frac{\partial f_N}{\partial \Gamma_1} \\ \vdots & & \ddots & & \vdots \\ f_1 \frac{\partial f_1}{\partial \Gamma_N} & + & \dots & + & f_N \frac{\partial f_N}{\partial \Gamma_N} \end{bmatrix} \tag{2.30}$$

and can be rewritten in terms of the Jacobian matrix as

$$\nabla P(\mathbf{\Gamma}) = [\mathbf{J}] \begin{bmatrix} f_1(\mathbf{\Gamma}) \\ f_2(\mathbf{\Gamma}) \\ \vdots \\ f_N(\mathbf{\Gamma}) \end{bmatrix} \tag{2.31}$$

Therefore, $\triangledown P(\mathbf{\Gamma})$ can be used as the gradient in the solver because

$$\nabla P(\mathbf{\Gamma}) \propto \nabla \|\mathbf{R}\| \tag{2.32}$$

Once the gradient is found, a line search is performed in the direction opposite of the gradient (the direction of steepest descent) until a local minimum in that direction is found. This new point is used as the new initial point. The process is repeated until the solver converges.

Steepest Descent is advantageous in that it is guaranteed to always progress down-hill and find a local minimum. Additionally, it usually makes good progress during the first few iterations. However, if the design space is eccentric, the convergence process may take a long time.

2.5.6 BFGS Update Solver

The ideal solver would begin by using steepest descent and would gradually switch to using the Jacobian. This would ensure that good progress would be made near the beginning of the iterations, and that the optimum would be quickly found when the iterations near convergence. Such methods exist and are called Rank 1

Update methods. These methods choose a direction to search by multiplying the gradient at the current solution by a direction matrix $\mathbf{O}$ as follows

$$\mathbf{s} = -\mathbf{O}\nabla f \tag{2.33}$$

$\mathbf{O}$ begins as the identity matrix, and is slowly transformed to the Hessian of the design space by storing gradients as it traverses the design space. When $\mathbf{O}$ is the identity matrix, the search direction is directly opposite of the gradient at the current solution. However, as the solver progresses, $\mathbf{O}$ becomes the Hessian, and is able to make faster progress toward the optimum.

Currently, the Broyden-Fletcher-Goldfarb-Shanno (BFGS) Update is considered to be the best update method. The direction matrix $\mathbf{O}$ for this method is found from

$$\mathbf{O}^{k+1} = \mathbf{O}^k + \left(1 + \frac{\left(\gamma^k\right)^T \mathbf{O}^k \gamma^k}{\left(\Delta\mathbf{\Gamma}^k\right)^T \gamma^k}\right)\left(\frac{\Delta\mathbf{\Gamma}^k \left(\Delta\mathbf{\Gamma}^k\right)^T}{\left(\Delta\mathbf{\Gamma}^k\right)^T \gamma^k}\right) - \frac{\Delta\mathbf{\Gamma}^k \left(\gamma^k\right)^T \mathbf{O}^k + \mathbf{O}^k \gamma^k \left(\Delta\mathbf{\Gamma}^k\right)^T}{\left(\Delta\mathbf{\Gamma}^k\right)^T \left(\gamma^k\right)} \tag{2.34}$$

where

$$\gamma^k = \nabla f\left(\mathbf{\Gamma}^{k+1}\right) - \nabla f\left(\mathbf{\Gamma}^k\right), \tag{2.35}$$

$$\Delta\mathbf{\Gamma}^k = \mathbf{\Gamma}^{k+1} - \mathbf{\Gamma}^k, \tag{2.36}$$

and k is the iteration number.

2.6 Flaps

In order to predict the aerodynamics of aircraft, the effects of control surfaces on the aircraft must be taken into account. Such effects can be accounted for by altering the lift, drag, and moment coefficients of wing sections with a deflected control surface. Equation (2.3) defines the local lift coefficient, C_{l_i}, as an arbitrary function of both the local angle of attack, α_i, and the local flap deflection, δ_i. The

drag and moment coefficients can also be defined as arbitrary function of the local angle of attack and flap deflection. This section describes the calculations of each.

2.6.1 Lift Coefficient

Phillips [11] suggests a simple way to calculate the increase in lift coefficient with flap deflection. A brief overview of the method is given here.

Suppose that an airfoil is at an angle of attack, α. If the lift slope, $C_{l\alpha}$, of the airfoil is known, the lift coefficient can be calculated as an angle multiplied by the lift slope

$$C_l = C_{l\alpha}[\alpha - \alpha_{L0}] \tag{2.37}$$

where α_{L0} is the zero-lift angle of attack of the 2D airfoil with no flap deflection. When a positive flap deflection, δ_f, is added, the camber of the airfoil is increased. The increase in lift can be approximated by

$$\delta C_l = C_{l\alpha}[\epsilon_f \delta_f] \tag{2.38}$$

where ϵ_f is the actual flap effectiveness and can be defined as follows:

$$\epsilon_f = \epsilon_{fi}\eta_h\eta_d \tag{2.39}$$

Here, ϵ_{fi} is the ideal flap effectiveness, η_h is the hinge efficiency, and η_d is a deflection efficiency. The ideal flap effectiveness is a function of θ_f.

$$\epsilon_{fi} = 1 - \frac{\theta_f - \sin\theta_f}{\pi} \tag{2.40}$$

θ_f is simply a geometric property of the wing and is a function of the ratio of the flap chord, c_f to the section chord, c.

$$\theta_f = \cos^{-1}\left(2\frac{c_f}{c} - 1\right) \tag{2.41}$$

The hinge efficiency, η_h, is a function of the ratio of the flap chord to the section chord. When this ratio is small, the efficiency is very low. However, as this ratio approaches 1, the efficiency approaches 1 in an asymptotic fashion. The hinge efficiency can be approximated as

$$\eta_h = 3.9598 \tan^{-1}\left[\left(\frac{c_f}{c} + .006527\right) 89.2574 + 4.898015\right] - 5.18786 \tag{2.42}$$

This is a numerical approximation of the graphical relationship presented by Phillips [11]. The hinge efficiency should be decreased by 20 percent for unsealed flaps.

The deflection efficiency, η_d, is a function of the deflection. At deflections less than 10 degrees, the efficiency can be assumed to be 1. However, above 10 degrees, the efficiency begins to drop linearly with deflection angle. The deflection efficiency can be approximated from the equation

$$\eta_d = -.0086\,(\delta) + 1.108 \tag{2.43}$$

which is also a numerical approximation of the graphical relationship presented by Phillips [11].

Even with the definitions above, various methods can be used to approximate the lift coefficient with varying angle of attack and flap deflection. It is of worth to be more specific about how the code presented here calculates the lift coefficient. In this code, the 2D airfoil data is used as the arbitrary function to calculate the lift coefficient with respect to angle of attack with no flap deflection. Additionally, the lift slope at the local angle of attack with no flap deflection, $C_{l\alpha,l}$, is used as the 2D airfoil lift slope. Thus, a flap deflection at a low angle of attack when the lift slope is at a maximum is more effective than a flap deflection near stall where the lift slope decreases. Equation (2.37) and Eq. (2.38) combine to produce

$$C_{l_i} = C_{l_i}(\alpha_i) + C_{l\alpha,l}[\epsilon_f \delta_f] \tag{2.44}$$

2.6.2 Drag Coefficient

The drag coefficient can also be approximated by an arbitrary function of the local angle of attack. Without a flap deflection, the 2D airfoil data is used as the arbitrary function.

$$C_{d_i} = C_{d_i}(\alpha_i) \tag{2.45}$$

When a flap deflection exists, the lift coefficient is first calculated, and the drag polar is then used as the relation to calculate the drag coefficient.

$$C_{d_i} = C_{d_i}(C_{l_i}) \tag{2.46}$$

The drag polar cannot be used when the lift coefficient caused by the flap deflection exceeds the maximum lift coefficient of the 2D airfoil without a flap deflection. In this case, the effect of the flap deflection is ignored, and the drag coefficient is approximated from the 2D airfoil data at the local angle of attack. Above stall, the flap is assumed to be totally ineffective, and the 2D airfoil drag coefficient is used regardless of the flap deflection.

2.6.3 Moment Coefficient

The moment coefficient is also effected by the application of flaps and can be approximated as an arbitrary function of both local angle of attack, α_i, and local flap deflection, δ_f.

$$C_{m_i} = C_{m_i}(\alpha_i, \delta_f) \tag{2.47}$$

Phillips [11] suggests simply adding a correction factor to the 2D moment coefficient at the local angle of attack as follows:

$$\delta C_{m_i} = C_{m,\delta}\delta_f \tag{2.48}$$

Using the ideal moment slope for thin airfoil theory, the change in moment slope with flap deflection, $C_{m,\delta}$, can be approximated by

$$C_{m,\delta} = \frac{\sin(2\theta_f) - 2\sin\theta_f}{4} \tag{2.49}$$

This value is simply multiplied by the flap deflection and added to the original moment calculated from the 2D airfoil data at the local angle of attack to find the total section moment coefficient.

2.6.4 Flaps Above Stall

Above stall it is assumed that the flaps have no effect and can be ignored in the lift, drag, and moment coefficient calculations. This can be assumed because the flow on the upper surface of a wing in stall separates, causing the flaps to lose their effectiveness.

2.7 Summary

A numerical method based on Prandtl's classical lifting line theory has been presented. Methods for solving the resulting system of equations have been discussed. Additionally, the treatment of flap effects below and above stall has been addressed.

Chapter 3

Numerical Blade-Element Model

A numerical method is presented as a low computational cost approach to modeling an induced propeller flowfield. This method uses blade element theory coupled with momentum equations to predict the axial and tangential velocities within the slipstream of the propeller, without the small angle approximation assumption common to most propeller models.

3.1 Nomenclature

B_d = slipstream development factor

b = number of blades

C_b = batter capacity in mAh

C_l = section coefficient of lift

c_b = blade section chord

D_p = propeller diameter

E_b = battery voltage (Volts)

E_m = motor voltage (Volts)

E_o = no load battery voltage (Volts)

G_r = motor gear ratio

I_b = battery current (Amps)

I_m = motor current (Amps)

I_o = no load motor current (Amps)

J = advance ratio

K_v = motor voltage constant (RPM/volt)

N = number of blade sections

N_m = motor RPM

N_p = propeller RPM

P_b = motor break power (Watts)

R_b = battery internal resistance (Ohms)

R_c = speed control operating resistance (Ohms)

R_m = motor resistance (Ohms)

R_p = propeller radius

r = radial distance from propeller axis

s = normal distance to propeller plane

T_m = motor torque (Nm)

T_p = propeller torque (Nm)

V_i = blade section total induced velocity

$V_{\theta i}$ = blade section induced tangential velocity

α = angle of attack to freestream

β_t = geometric angle of attack at propeller tip

η = motor and battery system efficiency

ϵ_i = blade section induced angle of attack

ϵ_∞ = blade section advance angle of attack

Γ = blade section circulation

κ = Goldstein's kappa factor

ω = propeller angular velocity

τ = throttle setting

θ = azimuthal angle of propeller

ζ_b = battery endurance (hrs)

3.2 History

The origins of blade element theory began in the late 1800s and continued development into the early 1900s. However, lack of the ability to account for the induced angle of attack which was apparent in experiments hindered the theory's

credibility. Lifting line theory became the credible source for calculating the forces on both fixed and rotary wings in the early 1900s because of its ability to model the induced velocity at each wing section. Later, research by Prandtl [12] and Goldstein [13] allowed for the development of an expression for the circulation about the blade, and the induced velocity was accounted for in the blade element theory. This theory is now used mainly for rotary wings as it allows for a fast calculation of the induced axial and tangential velocities in the plane of a propeller. However, it does not account for interactions between other fixed or rotary wings. Therefore, it is seldom used for fixed-wing aircraft analysis.

3.3 Assumptions

The blade element approach, coupled with a slipstream development factor based on momentum equations, to modeling the propeller flowfield implies a few underlying assumptions. These are discussed below.

- The axis of the propeller slipstream stays coincident with the axis of the propeller. This can be assumed if the induced axial velocity of the propeller is much greater than the propeller sideslip velocity.

- There is no mixing between the slipstream and the freestream velocities. No adjustments are made at the edges of the slipstream to account for mixing with the freestream. This is obviously a significant assumption, but accounting for these effects is beyond the scope of this initial-stage aerodynamic model.

- The helical trailing vortex sheet maintains a constant pitch.

- Finally, the resultant induced velocities at any distance behind the propeller are assumed constant with varying azimuthal angle. Therefore, although the induced velocity downstream from the propeller is a function of θ when the propeller is at an angle of attack, the *average* velocity at that radius and distance from the propeller is taken as the induced velocity.

3.4 Formulation

In order to predict the time-averaged slipstream behind a propeller, an induced velocity must be calculated immediately behind the propeller. This velocity is a function only of the radius if the propeller axis is in line with the freestream velocity vector, and a function of radius and azimuthal angle, θ, if the propeller is not aligned with the freestream. Phillips [11] presents an approach that does not constrain the freestream velocity to be aligned with the propeller axis. Thus, off-axis moments and forces from the propeller can be found. Dividing the propeller into N discrete intervals, the induced velocity at each radial blade element can be found by relating the section circulation to the section induced tangential velocity as shown in Eq. (3.1).

$$b\Gamma = 4\pi\kappa r V_{\theta i} \tag{3.1}$$

Substituting Prandtl's tip loss factor [12] for Goldstein's κ factor, the following equation is produced:

$$\frac{bc_b}{16r}C_l - \cos^{-1}\left(exp\left[-\frac{b\left(1-\frac{2r}{D_p}\right)}{2\sin\beta_t}\right]\right)\tan\epsilon_i \sin(\epsilon_\infty + \epsilon_i) = 0 \tag{3.2}$$

which can be numerically solved for ϵ_i. Once ϵ_i is known for a given blade section, the total induced velocity is found from

$$V_i = \frac{\omega r \sin\epsilon_i}{\cos\epsilon_\infty} \tag{3.3}$$

This velocity vector is then divided into its axial and tangential components. These components can be integrated to find the thrust and torque, respectively, of the propeller.

Once the induced axial and tangential velocities are known at the propeller plane, the flowfield behind the propeller can be estimated by applying conservation of momentum equations. The slipstream radius at a distance s behind the propeller is found by solving for the slipstream development factor suggested by McCormick:

[14]

$$B_d = 1 + \frac{s}{\sqrt{s^2 + R_d^2}} \tag{3.4}$$

where B_d is the development factor and approaches 2 as the distance from the propeller plane (s) approaches infinity. Using this radius, and applying conservation of mass and angular momentum as suggested by Stone [6], the development of the axial and tangential velocities throughout the slipstream are found.

3.5 Battery and Motor Properties

It is often helpful to predict the behavior of a battery, motor, and propeller combination. Blade element theory allows the thrust and torque of a propeller to be predicted. This torque must be matched by the motor to continue operation. Using a basic electric motor model, the required power of the motor in terms of voltage and current can be found.

Given the motor, battery, and speed control constants, K_v, G_r, R_m, I_o, R_b, E_o, and R_c, along with the speed control setting, τ, and the propeller torque, T_p, motor and battery variables can be found as follows.

$$T_m = \frac{T_p}{G_r} \tag{3.5}$$

$$I_m = .1047 K_v T_m + I_o \tag{3.6}$$

$$E_b = E_o - I_m R_b \tag{3.7}$$

$$I_b = \tau I_m \tag{3.8}$$

$$\eta_s = 1 - .078(1 - \tau) \tag{3.9}$$

$$E_m = \eta_s \tau E_b - I_m R_c \tag{3.10}$$

$$N_m = K_v \left(E_m - I_m R_m\right) \tag{3.11}$$

Iterations are performed until both the motor RPM and propeller RPM match. Once these values match, the motor break power, P_b, can be calculated as well as a

prediction for the battery endurance, ζ_b.

$$P_b = .14198 T_m N_m \tag{3.12}$$

$$\zeta_b = \frac{C_b}{1000 I_b} \tag{3.13}$$

This gives a reasonable prediction for the electrical characteristics of the motor, battery, and propeller combination.

3.6 Combined Model Assumptions

The numerical lifting line model and the blade element propeller model were combined to produce a complete algorithm capable of predicting propeller/wing interactions. A major design consideration in the development of the computer code was the intention of making the algorithm fast enough to link to a real-time simulator. In order to facilitate this need, a few assumptions within each model were made. These assumptions are explained in 2.3 and 3.3.

The combination of the two numerical models into a comprehensive model requires an additional assumption. In order to preserve the low-cost computational goal of the algorithm, it is assumed that the propeller aerodynamics affect the wing, but the wing aerodynamics do not affect the propeller. This allows for the combined wing and propeller models to first solve the propeller behavior and then solve for the aerodynamics of the wing in the resultant flowfield. No iterations need be performed between the flowfields of the wing and propeller, which provides for a faster solution.

Chapter 4

Results

4.1 Lifting Line Model

4.1.1 Below Stall

As a first check on the present numerical lifting line algorithm, inviscid estimates of wing lift coefficient for a swept wing in a uniform freestream were computed. The section lift coefficient was defined as a linear function of angle of attack, and the section parasite drag was set to zero. For this case, the algorithm exactly reproduces the results of a published numerical lifting line algorithm [5] as shown in Fig. 4.1.

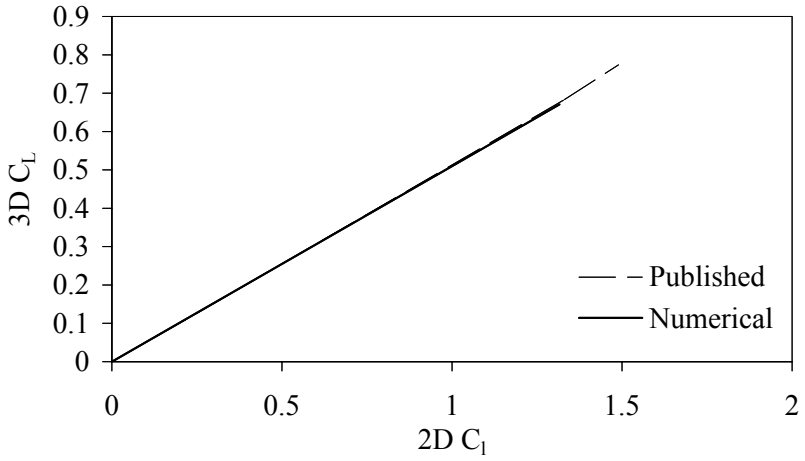

Figure 4.1: 3D wing C_L vs. 2D section C_l for a wing with sweep. Comparison to published lifting line results [5]

4.1.2 Above Stall

Lifting line theory is based on the assumption that at each spanwise section of the wing, the lift generated by the section circulation can be equated to the lift generated by a similar 2D airfoil. This works well for angles of attack below stall. However, above stall this assumption breaks down. Anderson [10] mentions that if the 2D airfoil data is known above stall, an "engineering solution" may be obtained using a lifting line algorithm. Additionally, Phillips [11] suggests that his numerical lifting line method can converge for a wing above stall if the system of equations is extremely underrelaxed. Others have studied the use of lifting line algorithms above stall and have made various observations. The results presented in this section support Anderson's claim that if the 2D airfoil data is known above stall, a reasonable estimate for the lift and drag on a 3D wing can be predicted. Additionally, the results presented here validate the claims of others as will be discussed.

Oscillations

Numerical solutions found for wings near or above stall have been found to have spanwise oscillations [15, 16] which have discouraged some from trusting these results. Von Karman is said to have proven that above stall, there are an infinite number of solutions to the lifting line equation [17]. This includes symmetrical and asymmetrical solutions. Additionally, the solutions have been shown to be greatly dependent on the initial guesses for the system [10]. Thus a numerical result of the lift distribution of a wing above stall should not be accepted as singularly viable.

One attempt to remedy the oscillatory problem was conducted by Mukherjee [16] who has shown that the algorithm can be "guided" to a more controlled solution with less oscillation by using a decambering approach. This author also has initial ideas on how the solution may be guided to a less oscillatory solution. However, it is beyond the scope of the current research and will not be considered here. Here, the oscillatory behavior is simply noted and quantified. Further research should be

conducted to better understand this behavior and to find methods of damping the oscillation within the solution.

Figure 4.2 shows resulting circulation distributions for a wing with an aspect ratio of 6 at seven post-stall angles of attack. Each circulation distribution was computed using 18 wing sections across the span in a cosine distribution. The 2D airfoil C_l used for the computation can be seen in Fig. 4.3.

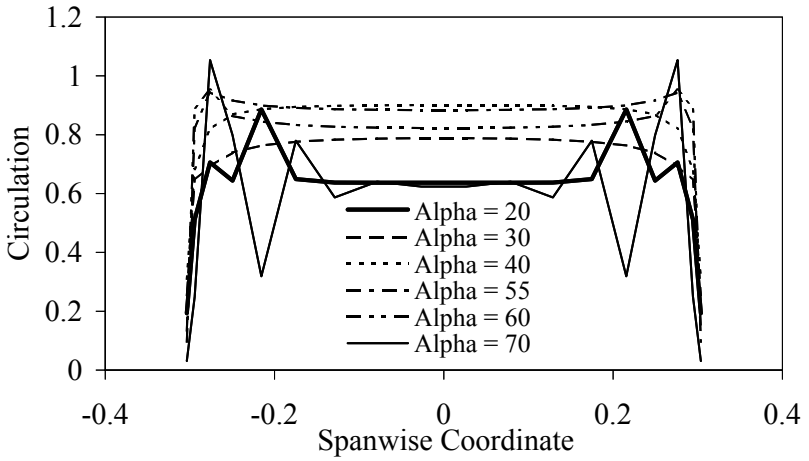

Figure 4.2: Circulation distributions for a wing with an aspect ratio of 6 at various angles of attack. Angles shown in degrees.

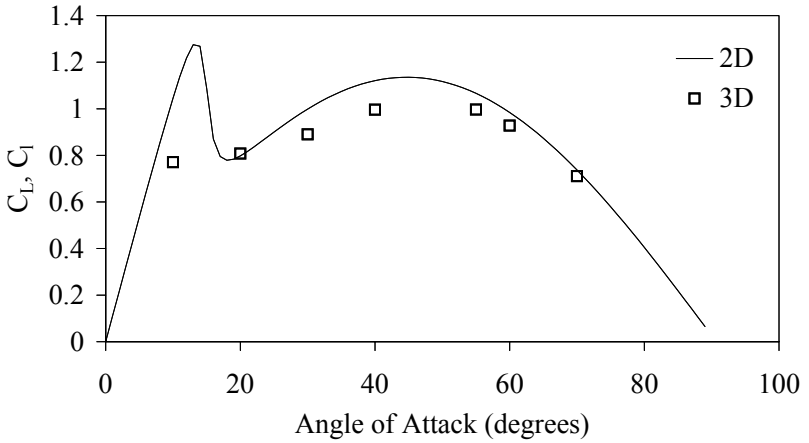

Figure 4.3: 2D C_l vs. α input and 3D C_L vs. α results on a wing with an aspect ratio of 6 with a grid density of 18.

Notice the oscillatory behavior of the circulation distribution above stall. Although the distributions are obviously not correct, the integrated lift across the wing matches closely to the expected total lift on the wing which can be seen in Fig. 4.3.

Spanwise Section Distribution Effects

The author has found the solution to be highly dependent on the spanwise section distribution used for the computations. It is assumed that this phenomenon has not been realized by others [10, 16] because their numerical models were not able to support various spanwise section distributions.

Figure 4.4 shows the converged circulation distributions for a wing with an aspect ratio of 6 with two different grid densities. Both of the grid densities follow a cosine distribution.

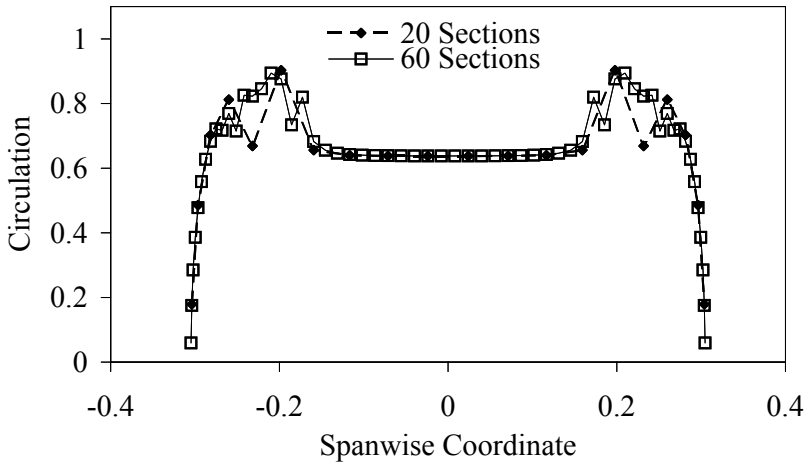

Figure 4.4: Comparison of the numerical circulation distributions for a wing with two different section distributions.

To understand the effect of spanwise section distributions on the solution, the lift distribution on a symmetrical wing with an aspect ratio of 6 was solved for 13 angles of attack between 0 and 90 degrees. At each angle of attack, the wing was analyzed using 46 different distributions. These section distributions varied from 10 spanwise sections to 100 spanwise sections by increments of 2. Each of

the section distributions followed a cosine distribution. At angles of attack where the 2D airfoil data has a positive lift slope, the Jacobian solver was used. At all other angles of attack, the Steepest Descent solver was used. If the solver did not converge within 1000 iterations, it was halted. Only those solutions which reached a "converged" state, meaning that the residual described in (2.5) was driven sufficiently near zero, were considered. Additionally, any solutions which resulted in a total lift coefficient which varied by more than 100 percent from the 2D airfoil data were not considered. Figure 4.5 shows which section distributions returned solutions that met these criterion.

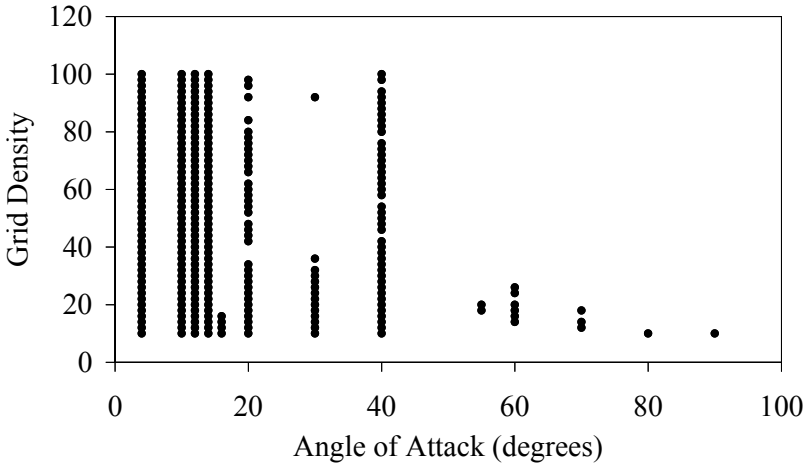

Figure 4.5: Wing section distributions which yielded acceptable results.

At each angle of attack, all of the converged solutions from the varying grid densities were averaged and their variance was quantified. Figure 4.6 shows the resulting average 3D wing lift coefficients at each angle of attack compared to the 2D input lift coefficient data. Figure 4.7 shows the variance in the averaged 3D wing lift coefficients at each angle of attack.

Notice that the variance below stall is extremely small while the variance just past stall is significantly higher. This immediate post-stall region is possibly the most difficult range of angles of attack to predict because in this region the wing is

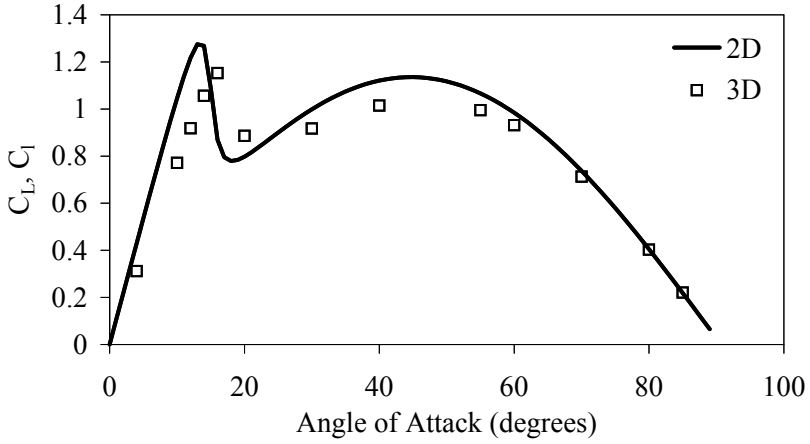

Figure 4.6: 2D and 3D C_L vs. α values for a wing with an aspect ratio of 6.

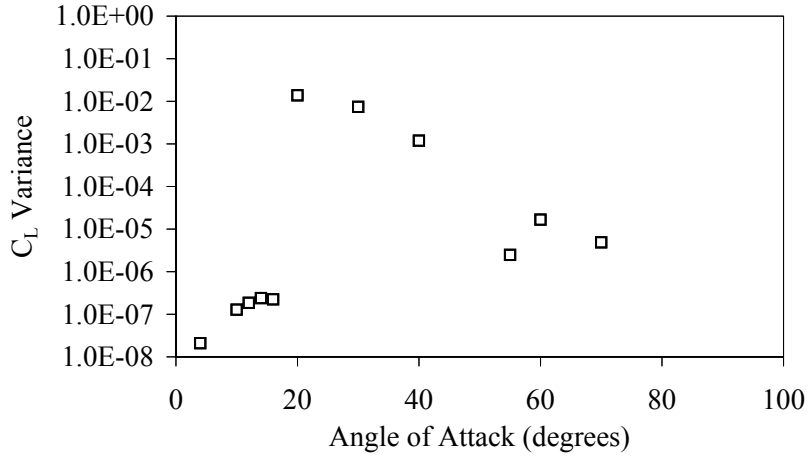

Figure 4.7: Variance in computed 3D lift coefficients over a range of angles of attack.

only partially stalled. At higher angles of attack where the wing is fully stalled, the variance in the solutions seems to drop. However, this drop in variance must also be partially attributed to the fact that at extremely high angles of attack, only a few grid densities converged. Still, it is significant that the variance in these solutions at high angles of attack is quite small.

From the data presented, we can conclude that although the variances in the solutions above stall are greater than those below stall, the total lift calculated from a circulation distribution solution above stall is a practical estimate for the total lift on the wing, even if the circulation distribution contains oscillations.

Lifting Line Limitation

At this point, an insightful realization about the limitations of the lifting line theory is worthy of note. Namely, that as a finite wing approaches 90° angle of attack, the lifting line theory is less able to take 3D effects into account in the lift, drag, and moment calculations.

This realization came as a result of a study of drag coefficients above stall. A 2D airfoil usually has a drag coefficient of about 2 at 90° angle of attack. However, the drag coefficient of a finite wing at 90° is usually around 1.2. Figure 4.8 compares the 2D drag data published by Pope [18] and used in the current model with the finite wing results for a wing with an aspect ratio of 5.536. Notice that the finite wing drag coefficient nears the 2D airfoil drag coefficient at high angles of attack. At 90°, where the 3D drag should be significantly lower than the 2D drag, the lifting line model predicts the drag to be the same as the 2D airfoil.

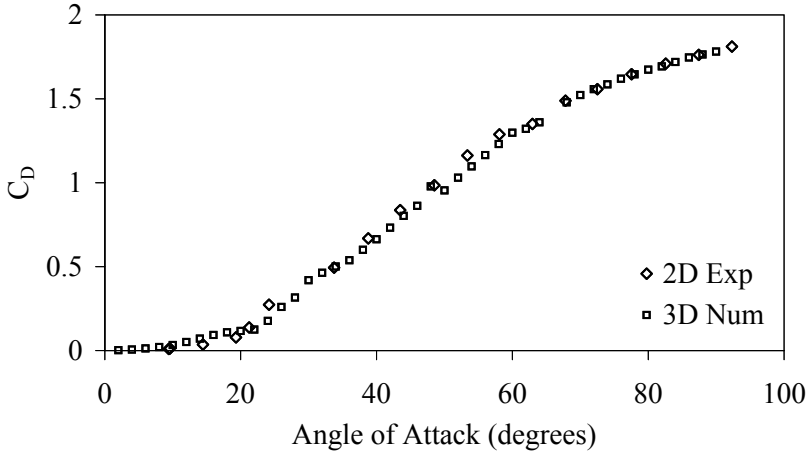

Figure 4.8: Experimental vs. numerical results for a 2D airfoil and a finite wing of aspect ratio 5.536 respectively.

The reason for this phenomenon can be understood by understanding the effect of circulation across the wing. If a portion of the wing is at an angle of attack near 90°, it has no circulation, and thus produces no downwash on other sections of the wing. The drag coefficient at any given section of the wing is calculated from the

local angle of attack. Therefore, if there is no downwash, the local angle of attack is the same as the freestream angle of attack, and the 2D airfoil drag coefficient is taken as the section drag coefficient. This means that as the 3D wing approaches 90° angle of attack, the 3D drag coefficient should likewise approach the 2D drag coefficient data, which is the case in the numerical results presented in Fig. 4.8.

This phenomenon is the same for lift and moment calculations. Therefore, as a finite wing nears 90°, its lift, drag, and moment calculations using lifting line theory approach that of its 2D airfoil. This trend can be seen in Fig. 4.3 and Fig. 4.6. Notice that as the wing approaches 90° angle of attack, the 3D results increasingly match the 2D results. This behavior can also be seen in the results presented in the following section. Similar results were found for moment calculations.

It is important to realize that this characteristic of lifting line theory is a result of the lift on a wing section (which is directly proportional to the circulation of the wing section) approaching zero at 90°. Thus, if an airfoil had 2D lift characteristics that approached zero at 50° rather than at 90°, this phenomenon would occur near 50° rather than at 90°.

4.1.3 NACA 0015 Test Case

To validate the model above stall, numerical results were compared to experimental values published by Critzos [19] and Anderson [10] for a NACA 0015 airfoil. Critzos published 2D lift, drag, and moment data taken by Pope [18] whose original publication was not readily available. However, Critzos reports that the data was taken at a Reynolds number of 1.23×10^6 and that the data was published without correction factors because the experimentalists found (through some tests and assumptions) that correction factors were not necessary. Anderson published numerical and experimental lift data for a finite wing with an aspect ratio of 5.563 from 0° to 50° at a Reynolds number of 2×10^6. However, he does not reveal the 2D data used for his numerical model. Thus Pope's 2D data was used as input to the current numerical model and the results were compared to Anderson's experimental and numerical results. Figure 4.9 compares the 2D data from Pope and the 3D numerical results

of the current model with the 3D experimental and numerical results published by Anderson.

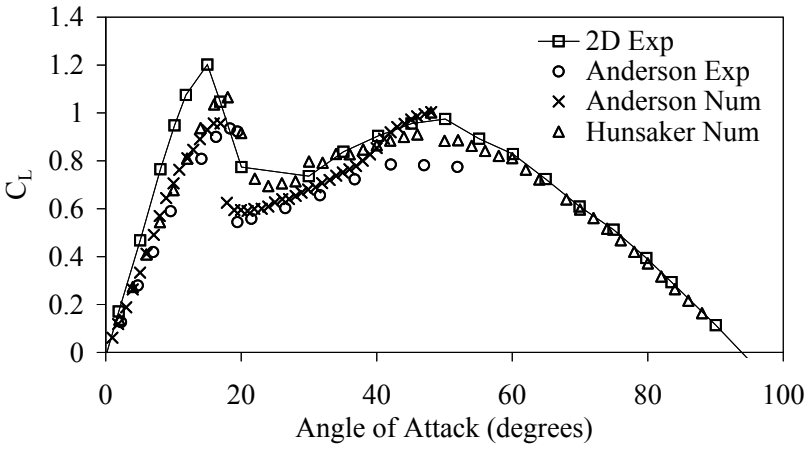

Figure 4.9: Experimental vs. numerical results for a finite wing of aspect ratio 5.536.

From the discrepancy between Anderson's finite-wing numerical results and the numerical results of the current model, it is apparent that Anderson's 2D airfoil lift data was slightly different than Pope's lift data. This can partly be attributed to the difference in Reynolds numbers of the two data sets. However, below 12°, the current model matches Anderson's experimental values better than his own finite-wing numerical model does. Notice that as Anderson's numerical results approach 40°, his numerical model seems to diverge and over-predict lift. However, the results of the numerical model presented here show that this model is capable of predicting reasonable values for lift across the entire regime of angles of attack.

4.1.4 Upstream Velocity Effects

To determine the ability of the model to predict the effects of uniform flow and irrotational slipstream flow, results are compared to the experimental data of Stuper [20]. (The ability of the lifting line model to predict rotational slipstreams is discussed in 4.3.) In these experiments, conducted in the 1930's, the aerodynamics of a finite wing were investigated in the presence of a slipstream. A Göttingen 409

airfoil section was employed on a rectangular wing of aspect ratio four (0.8 m span, 0.2 m chord) with circular end caps of diameter 0.32 m. Precautions were taken in the experimental setup to ensure that the slipstream produced by the 0.12 m diameter jet was both uniform and non-rotational. The freestream velocity was nominally 30 m/s, with jet speeds of 35.4 m/s and 40.8 m/s, representing 18% and 36% velocity increases in the slipstream, respectively.

For the numerical model, the 2D section lift behavior as a function of angle of attack is required. This behavior can be obtained either numerically or experimentally. Experimental results for the Göttingen 409 airfoil were not readily found in the literature, so instead a 2D incompressible Reynolds-Averaged Navier-Stokes (RANS) solution was used. For this, a pressure-based, segregated finite-volume solver was employed. In terms of the solution/discretization procedure, the convective terms were computed using a second-order upwind discretization, while the viscous terms were discretized using a second-order central discretization. Pressures were interpolated to the cell faces using a second-order interpolation scheme, and pressure-velocity coupling was achieved using the common SIMPLEC algorithm. Figure 4.10 shows the grid-converged results at Re$= 406,000$ using the Spalart-Allmaras [21] turbulence model. Although it is not expected that this model predicts the behavior beyond stall with a large degree of accuracy, it provides sufficiently accurate behavior in the absence of experimental data.

The end caps employed in Stuper's experiments significantly affect the lift behavior of the wing. To represent these circular caps in the computational model, vertical rectangular wing sections were included at the wing tips. Great care was taken to ensure that the effects of these rectangular surfaces correctly represented the effects of the circular caps. Figure 4.11 illustrates the numerical geometry, showing the wing and representative size of the slipstream. Note that the chord-wise lines represent the distribution of the 2D spanwise wing sections.

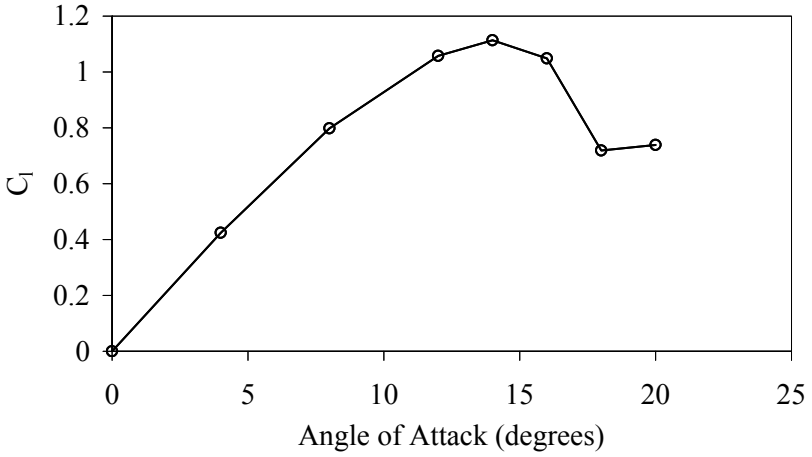

Figure 4.10: C_L vs. α for the Göttingen 409 airfoil at Re= 406,000 as predicted by the RANS equations.

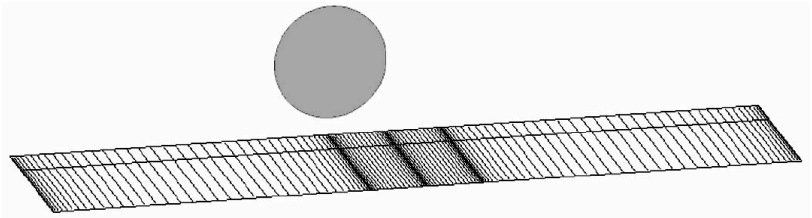

Figure 4.11: Computer model of the finite wing geometry showing the distribution of the spanwise sections. The circular disk illustrates the size of the jet relative to the wing.

Uniform Flow

As an initial check to the model, a uniform flow condition was tested. Figure 4.12 shows a comparison of the numerical solutions to the experimental C_l distributions at three angles of attack for the case of uniform flow. The similarity in behavior near the tips indicates that the rectangular surfaces accurately model the effects caused by the circular end caps used in the experiments. Note that the C_l distribution across the entire wing at both 4° and 12° angle of attack agree very well. At $\alpha = 8°$, however, the magnitude of the lift forces are under-predicted. This discrepancy is a result of a "jump" in the experimentally measured lift that occurs near $\alpha = 8°$ which can be seen throughout much of Stuper's data. This jump is not predicted by the 2D RANS solution used as an input into the lifting line algorithm and is assumed to be an error in the experimental data.

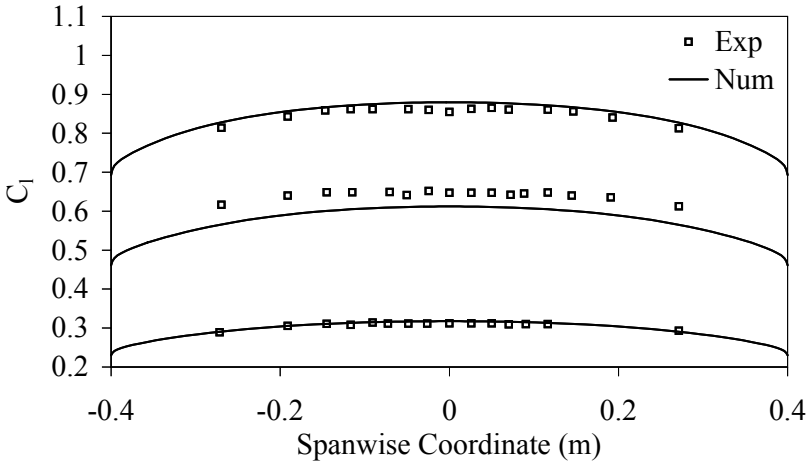

Figure 4.12: C_l distribution across the wing at three angles of attack, $\alpha = 4$, $\alpha = 8$, and $\alpha = 12$, with a uniform freestream velocity. Experimental values published by Stuper [20].

Irrotational Slipstream

Once the uniform flow condition had been tested, the ability of the model to handle irrotational slipstream flow could be tested. The experimentally measured upstream velocity profiles were used as inputs to the numerical model, and are shown in Fig. 4.1.4. These profiles are altered slightly from the experiments in that they represent symmetrically "averaged" profiles (the measured profiles exhibit some asymmetric behavior that is ignored in the numerical model). Note that a significant velocity deficit occurs near the edge of the slipstream. Stuper attributes this deficit to viscous effects on the jet nozzle placed upstream of the wing.

Using the nonlinear airfoil section lift behavior obtained from the RANS equations, the upstream velocity profiles obtained from the published experiments, and the geometry shown in Fig. 4.11, lift distribution results were obtained at three different angles of attack for both the 18% and 36% jets. The numerical solution required 19 Newton iterations to converge—about six seconds of CPU time on a Pentium 4 PC—for the worst case (36% jet at $\alpha = 8°$). The resulting lift distributions are shown in Fig. 4.14 and Fig. 4.15 along with the experimental values.

Overall, the numerical analysis shows good agreement with the experimental data. At $\alpha = 4°$, the numerical results appear to lie within the uncertainty of the

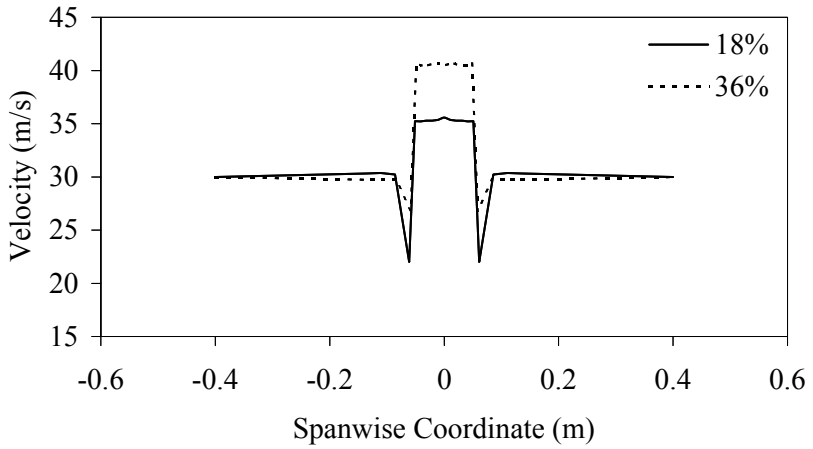

Figure 4.13: Upstream velocity profiles for 18% and 36% increase in freestream velocity in the slipstream, based on the measurements of Stuper [20].

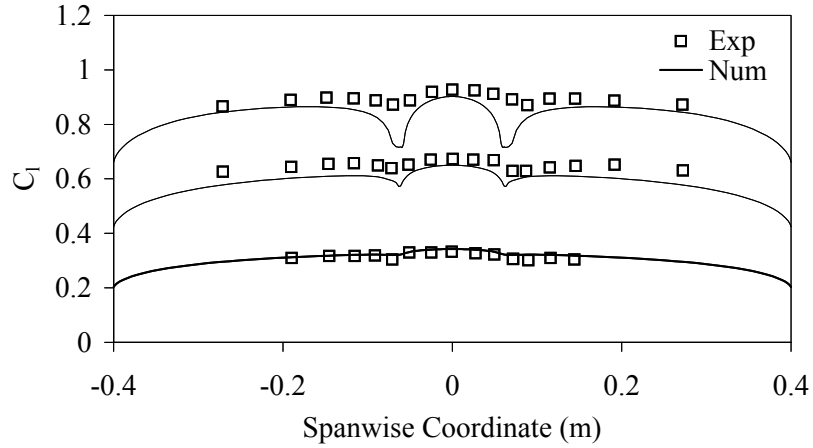

Figure 4.14: C_l distribution along the span for slipstream velocity 18% at three angles of attack, $\alpha = 4$, $\alpha = 8$, and $\alpha = 12$. Experimental values published by Stuper [20].

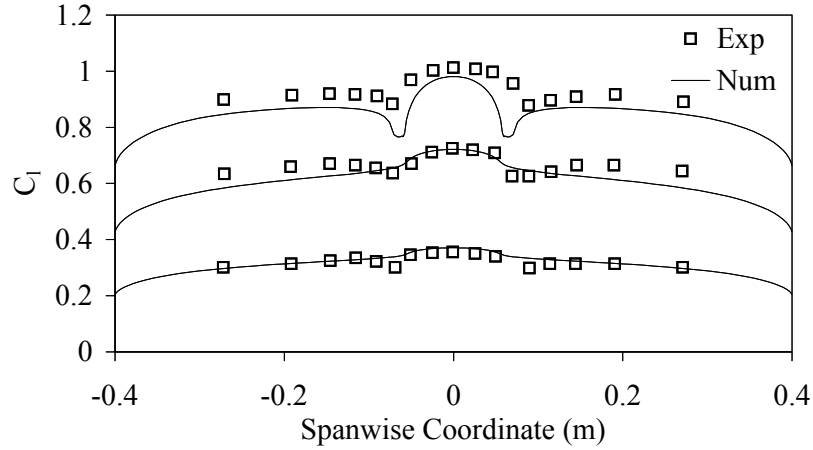

Figure 4.15: C_l distribution along the span for slipstream velocity 36% at three angles of attack, $\alpha = 4$, $\alpha = 8$, and $\alpha = 12$. Experimental values published by Stuper [20].

experimental data for both jet velocities. With increasing angle of attack, it appears that the deficit in velocity at the edges of the jet have a greater effect on the numerical results than the experimental results. This is noticeable from the large dips in the numerical results near the edge of the jet. These dips vary from the experimental results by about 12 to 16%.

Also of note is that the dips deviate more from experimental values when the wing is at a higher angle of attack. It should be remembered that no mixing between the jet velocity and the freestream velocity is modeled, which phenomenon could be causing the difference between the numerical and experimental results. The reader is reminded that the lifting line method calculates the lift from a section of wing purely by the incoming velocity experienced at the quarter chord of the wing. At higher angles of attack in experimental setups, this incoming velocity may vary from the given jet velocity because of boundary conditions present with the actual 3D wing. Thus, it is expected that viscous effects would cause the experimental results to be less agitated by a deficit in velocity than the numerical results.

It is also worth noting that at both 8° and 12° angle of attack, the experimental C_l values outside of the slipstream are noticeably higher (about 5%) than the numerical results. This phenomenon could also be caused by mixing or other pressure effects caused by the slipstream which are not accounted for in the numerical model.

It is apparent that the circulation distributions are more elliptically shaped at the tips of the wing. This stands to reason as the high circulation strengths within the jet profile have less effect on the outer edges of the wing because of distance. Thus, near the center of the wing, large amounts of downwash are experienced by the wing sections. This downwash, along with the deficit in velocity at the edge of the jet causes the circulation dip in the numerical results.

Also of interest is the overall C_L vs. α behavior for the finite wing with and without the slipstream. Figure 4.16 shows the experimental and numerical results for the coefficient of lift over a range of angles of attack. Note that the numerical model matches the data very well at angles of attack below stall. The numerical analysis predicts an increase in overall lift with increasing jet velocity which agrees with the

experimental data. The jump in the experimental C_L measurements at $\alpha = 8°$ is noticeable here. As stated previously, this jump was not found in the 2D RANS results.

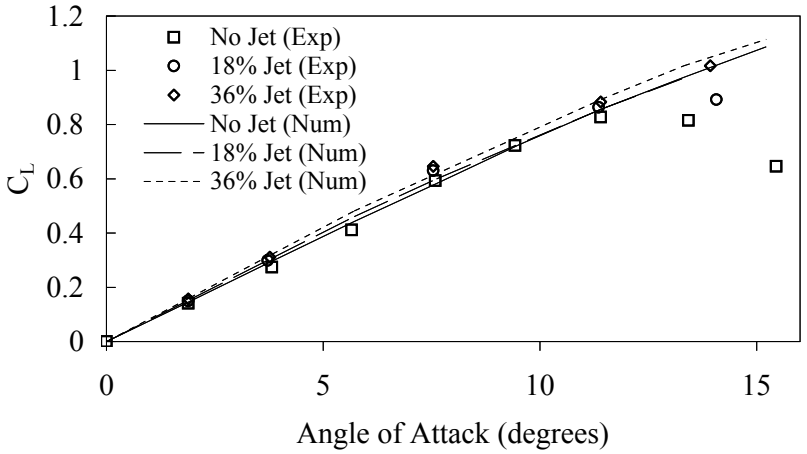

Figure 4.16: Overall C_L vs. α for the finite wing. Experimental values published by Stuper [20].

4.2 Propeller Model

Propellers are often characterized by only a diameter and pitch. However, propellers include many other significant (and often proprietary) parameters such as chord distribution, airfoil geometry, pitch offset, and pitch washout. These additional parameters are not usually included in published results. Therefore, it is often necessary to make a number of assumptions when modeling the aerodynamic characteristics of propellers. Basic assumptions were made in comparing the subsequent numerical results to experimental data and are noted where appropriate.

4.2.1 Total Thrust

Results from the model are first shown vs. experimental results published by Kotb [22]. Kotb included many important parameters in his paper, which allowed for accurate propeller parameters to be used in the numerical model. However, airfoil lift

and drag characteristics were not published, and are here assumed to be similar to a NACA 0012 airfoil. Figure 4.17 displays the numerical vs. experimental values for coefficient of thrust vs. advance ratio. The numerical model appears to be slightly optimistic across the entire range of tested advance ratios. This could be due to the fact that the model makes no adjustment for mixing with the freestream at the boundaries of the propwash. The lack of modeling the mixing phenomenon is apparent in subsequent plots.

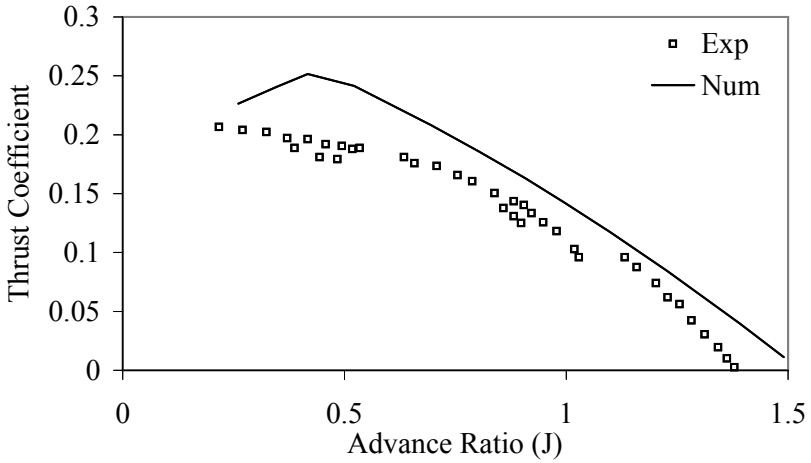

Figure 4.17: Experimental and numerical results for thrust coefficient vs. advance ratio. Experimental values published by Kotb [22].

In situations where the propeller is at an angle of attack to the freestream, the thrust varies azimuthally around the propeller. To check the accuracy of the off-axis model, results were compared to experimental results cited by McCormick [7]. Figure 4.18 shows how the ideal power required by the propeller varies with induced velocity and angle of attack. The velocity axis is normalized by the induced velocity under static conditions and the power axis is normalized by the power required to produce the same thrust under static conditions.

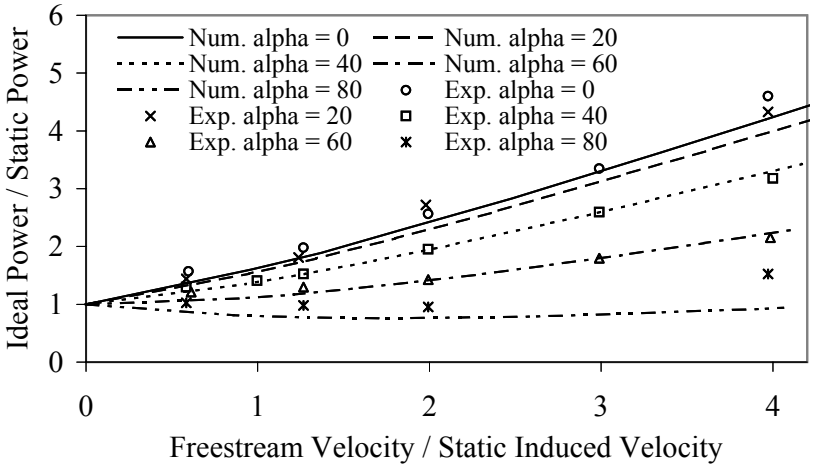

Figure 4.18: Required ideal power vs. velocity for constant thrust. Published data cited by McCormick [7].

4.2.2 Velocity Profiles

Figure 4.19 displays the numerical axial and tangential velocities predicted by the model vs. the time averaged experimental velocities published by Kotb [22]. The velocities are normalized by the freestream velocity. The lack of mixing with the freestream is obvious in these plots, as the numerical results peak near the edges of the propeller, rather than tapering off into the freestream. Further discrepancies between the two sets of data could be caused by the airfoil characteristics assumption.

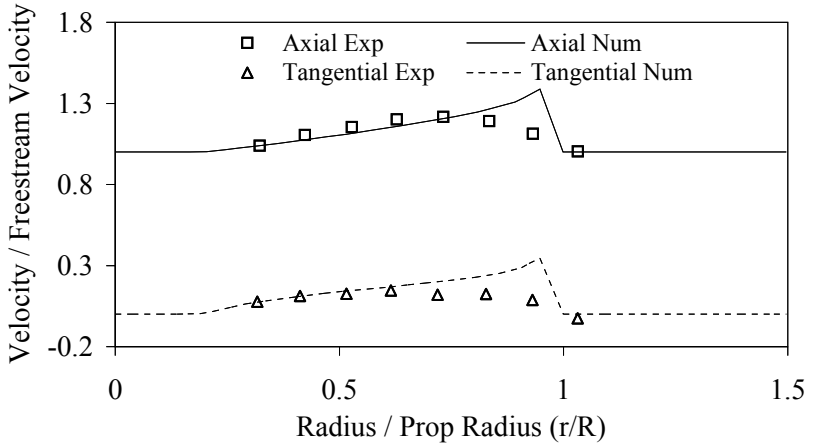

Figure 4.19: Normalized time-averaged velocities behind propeller vs. normalized propeller radius. Experimental values published by Kotb [22].

Figure 4.20 and Fig. 4.21 display the numerical results vs. the time averaged experimental data taken by Lepicovsky [23]. Only basic parameters of the experimental propeller were included in the publication, so two assumptions were made: 1) the chord has an elliptical distribution, 2) The airfoil has lift and drag characteristics of a NACA 0012. From the deficit in the predicted velocity profiles in Fig. 4.20, it is assumed that the propeller had an undisclosed pitch offset. By adding a pitch offset of 10 degrees, Fig. 4.21 was produced. Again, the lack of slipstream interaction with the freestream is apparent in the numerical model. However, the basic numerical velocity profiles are very similar to the experimental results.

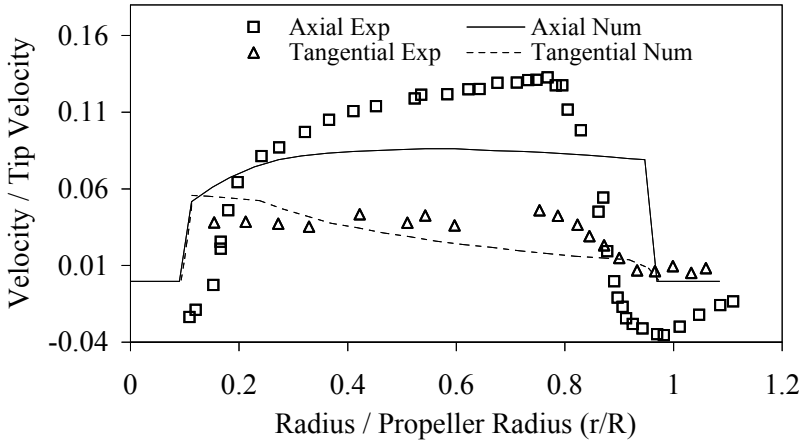

Figure 4.20: Normalized time-averaged velocities behind the propeller vs. normalized propeller radius. Experimental values published by Lepicosvsky [23].

4.2.3 Slipstream Profile

Figure 4.22a displays the numerical model predictions of the slipstream radius (white line) on the experimental data taken by Nozicka [24]. The data was taken at an advance ratio of 0 (static thrust condition) and reveals the strong slipstream contraction at static thrust conditions. Figure 4.22b displays the numerical model velocity field behind the propeller. The color coding of each of the two figures are referenced according to the color scale at the right of Fig. 4.22b which is in units of m/s.

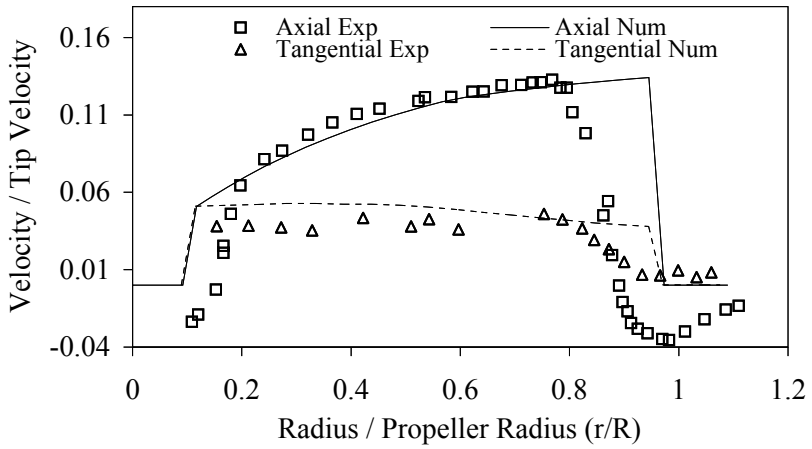

Figure 4.21: Normalized time-averaged velocities behind the propeller vs. normalized propeller radius. Experimental values published by Lepicosvsky [23].

From the figures it can be noted that the velocity magnitudes within the slipstream of the numerical solution match experimental data quite well. The slipstream radius of the numerical model appears to become more accurate to the experimental data as it moves further downstream. Other cases were tested at various advance ratios with similar results. Again, it is apparent that no mixing with the freestream is modeled.

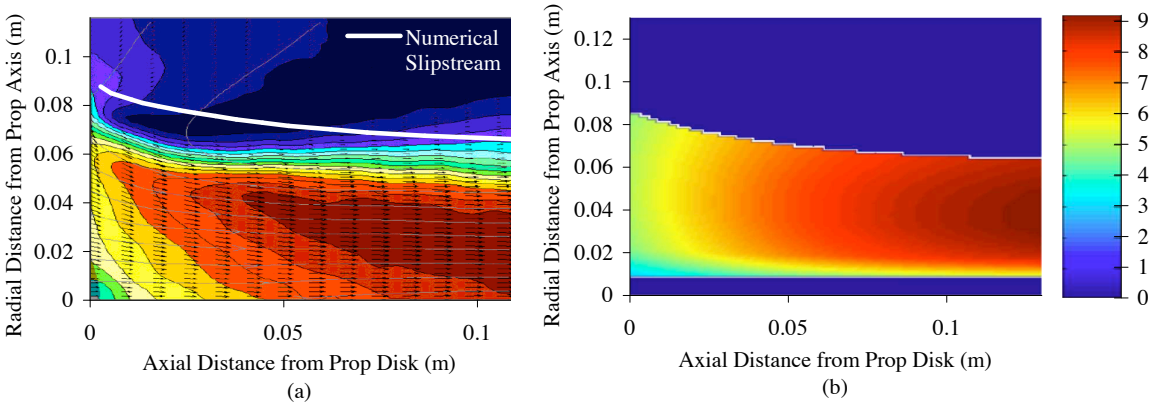

Figure 4.22: (a) Experimental axial velocity flowfield of a propeller at an advance ratio of zero as measured by Nozicka [24], overlaid with the numerical prediction of the slipstream edge. (b) Numerical prediction of the flowfield of a propeller at an advance ratio of zero. The color bar at the right has units of (m/s) and is applicable to both figures.

4.3 Combined Models

Finally, the numerical propeller and wing aerodynamic models are integrated into a single model to simulate the effects of propwash on the lift distribution along a finite wing. The same wing geometry used by Stuper [20] presented in the previous section is employed here (0.8 m span, 0.2 m chord). The propeller used in the experiments and numerics has a diameter of 15 cm and a pitch of 6 cm. The propeller was placed in the model 12.5 cm in front of the wing quarter chord and rotated at an advance ratio of 0.15 in the 30 m/s freestream. Figure 4.23 shows the resulting prediction for the C_l distribution across the wing.

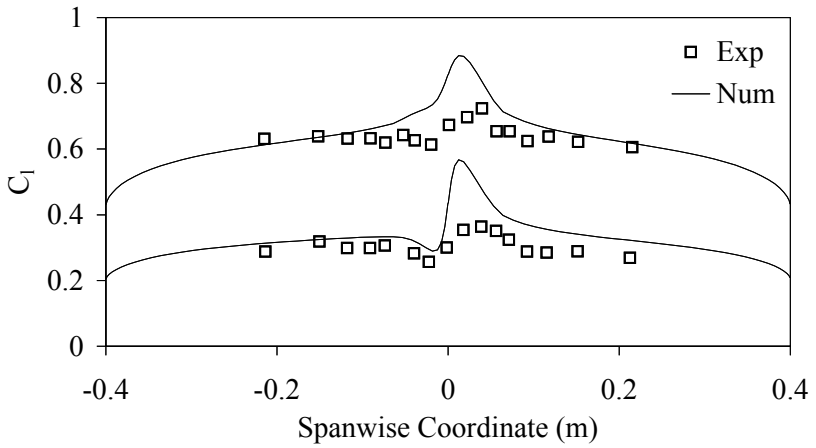

Figure 4.23: C_l distribution along the span of a wing in a propeller slipstream. Experimental values published by Stuper [20].

Note that the numerical results are qualitatively correct, but quantitatively optimistic. It should be noted that only standard pitch and diameter values are presented for the propeller used in the experiments. However, the actual propeller used in the experimental setup is not readily available, and thus assumptions were made. It is likely that a more accurate representation of the propeller would result in better agreement with the experimental data (although it is not expected to completely resolve the discrepancies in magnitude seen in the figure).

It is also possible that the numerical lifting-line approach implemented in the wing aerodynamic model is over-predicting the additional lift induced by the propeller. To understand this possibility, the reader is reminded that rotational velocities within the slipstream model increase as the slipstream contracts to preserve angular momentum. Thus, the leading edge of the wing is at a lower angle of attack than the quarter-chord of the wing. The lifting line model predicts aerodynamics from a single incoming velocity vector placed at the quarter chord, and it is assumed that the entire wing section is at a similar angle of attack. However, in a real-life scenario where viscous and boundary conditions affect the slipstream, the rotational flow caused by the propeller is damped out over the chordwise length of the wing. Thus, it is possible to imagine that the leading edge of the wing experiences the highest angle of attack and that the incident angle of attack decreases along the chordwise length of the wing. Modeling such boundary condition effects are beyond the scope of this project. However, as an initial modeling tool for wing and propeller interaction, the lifting line model combined with the blade element propeller model produces reasonable results.

Chapter 5

6 DOF Simulator Application

A compelling advantage of a low computational cost aerodynamics model is its ability to be linked to a flight simulator. In this way, autopilot controllers can be realistically tested and tuned on various airframes before being tested on expensive and fragile hardware in the field. This allows for the majority of the autopilot code testing to be accomplished in a virtual world before using the autopilot functions on actual airframes. Thus, the combined propeller and aerodynamics model was used to enhance the accuracy of a 6 degree of freedom (DOF) simulator written by Nathan Knoebel.

Originally, simple flight mechanics equations (which can be found in almost any mechanics or controls book [25, 11]) were used in the simulator to predict the aerodynamic loads on airframes in horizontal flight. Similar methods [26] were used to predict these forces and moments during hover modes. These simplified equations are based on aerodynamic coefficients often unknown about an airframe. Once the current aerodynamic model was completed, it was used to predict the aircraft coefficients of an airframe currently used for experimentation. With these coefficients, the 6 DOF simulator is able to run real-time with relatively accurate aerodynamic forces and moments.

The speed of the aerodynamics model also allowed it to be linked directly to the simulator for almost-real-time (ART) force updates. This provides for more accurate aerodynamic forces and moments to be computed for various flight regimes rather than relying on aerodynamic coefficients calculated for a steady-level flight regime to be used during other flight conditions such as climbing, banking, descending, etc.

Figure 5.1 through Fig. 5.6 compare the aerodynamic forces and moments in airframe coordinates of the two aerodynamic models. The first model is based on the simplified mechanics equations with aerodynamic coefficients, and the second model is the ART full aerodynamic modeling results. These ART full results were computed using the "Jacobian" solver for the system of equations. Similar (although less accurate) results can be achieved by using the "Best Linear" solver. Figure 5.7 shows the aircraft states for the computed flight regime. This flight period represents a horizontal launch and rolling climb of the aircraft.

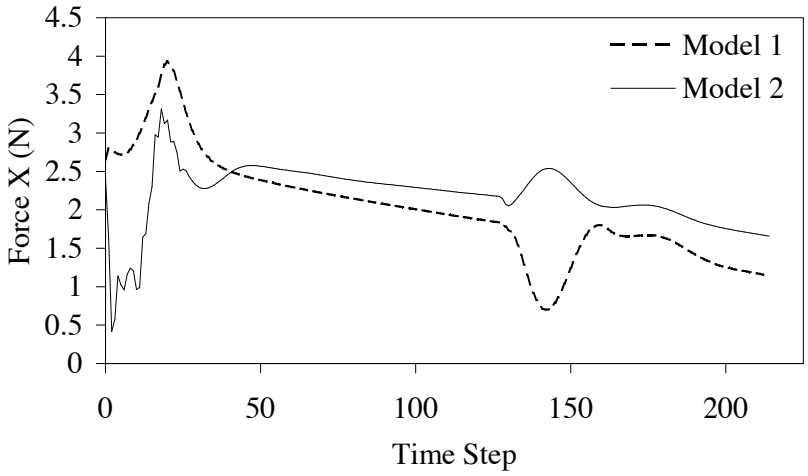

Figure 5.1: Predicted aerodynamic force in the x direction on the aircraft using each model.

Three significant observations can be made from the plots presented.

- First, there is a noticeable offset between each of the models throughout most of the plots. This can partially be attributed to the fact that the coefficients for the aircraft must be calculated at a set angle of attack. Model 1 uses these coefficients in a linear manner to predict the forces and moments at all other angles of attack while Model 2 uses the real-time angle of attack to predict the forces and moments.

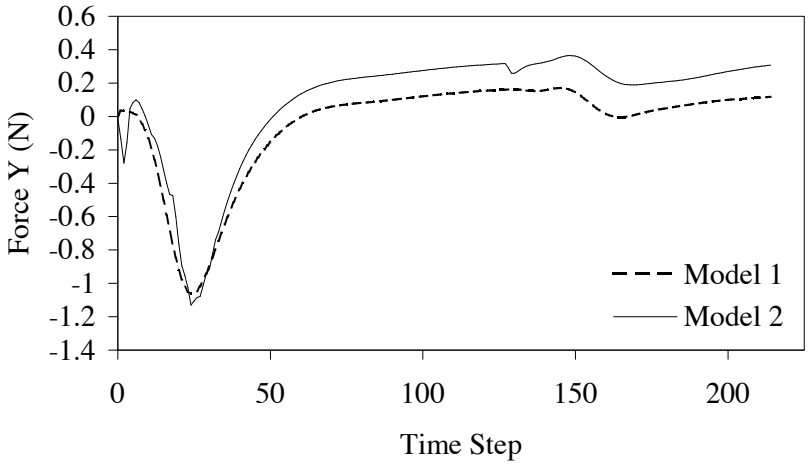

Figure 5.2: Predicted aerodynamic force in the y direction on the aircraft using each model.

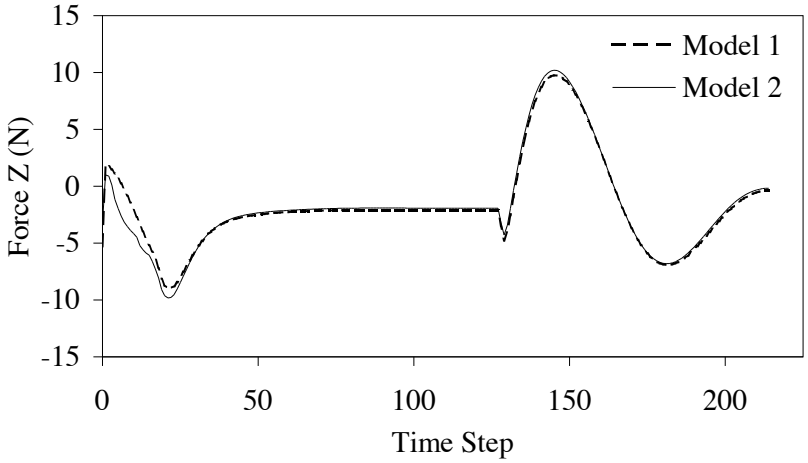

Figure 5.3: Predicted aerodynamic force in the z direction on the aircraft using each model.

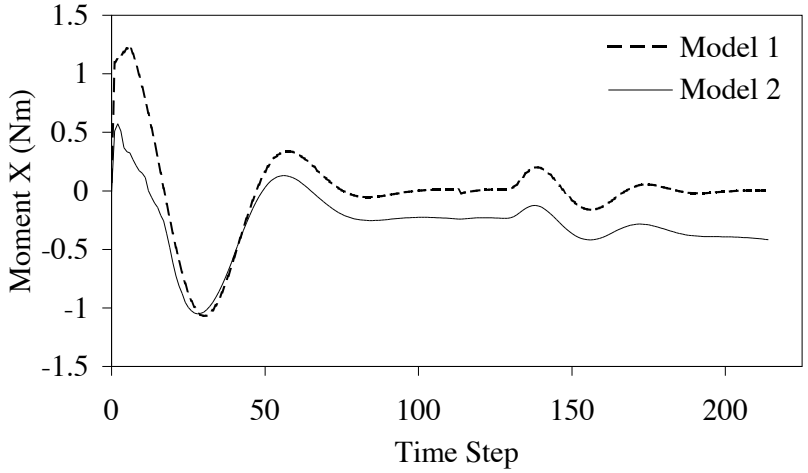

Figure 5.4: Predicted aerodynamic moment about the x axis of the aircraft using each model.

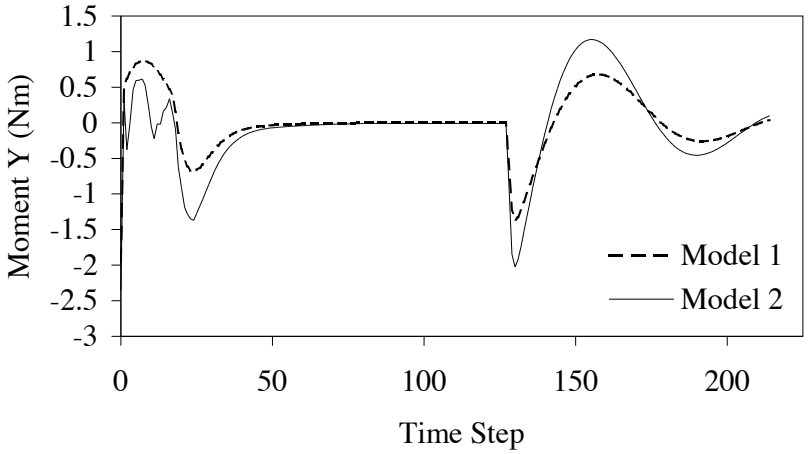

Figure 5.5: Predicted aerodynamic moment about the y axis of the aircraft using each model.

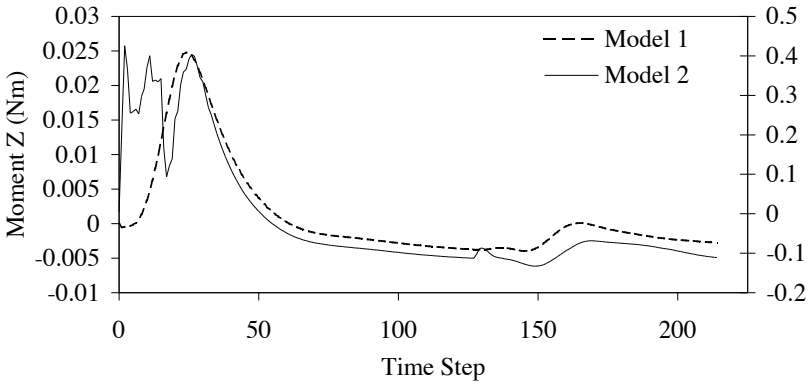

Figure 5.6: Predicted aerodynamic moment about the z axis of the aircraft using each model. The left y axis corresponds to model one and the right y axis corresponds to Model 2.

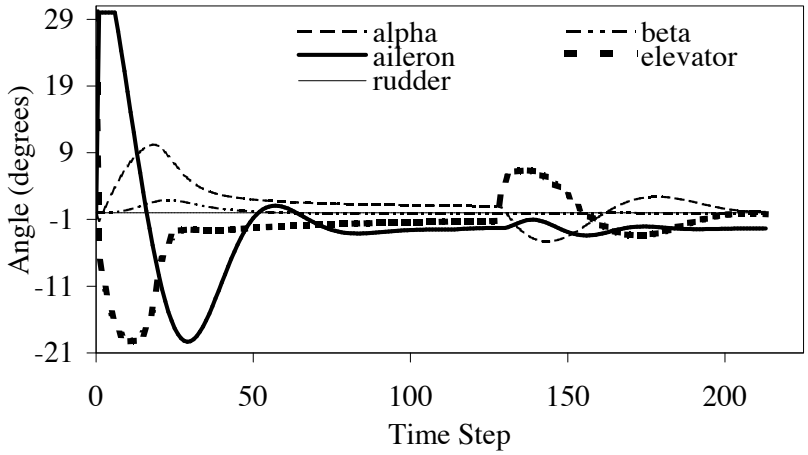

Figure 5.7: Deflections and states of the aircraft.

- Second, Model 1 is virtually unable to predict drag due to elevator and aileron deflections. This can be seen by noticing that the drag predicted from Model 1 near the beginning of the flight is much lower than the drag predicted by Model 2. During this time there are significant elevator and aileron deflections which naturally cause drag. Model 1 uses only a single coefficient to predict the drag due to elevator deflection and no coefficient to predict the drag due to aileron deflection. In fact, this coefficient has a positive sign, which results in a drag force when the elevator is positively deflected and a thrust force when the elevator is negatively deflected. Therefore, in the first few moments of this flight, when the elevator is negatively deflected, Model 1 shows more force in the x direction than Model 2, which can be attributed to this positive drag coefficient.

  This limitation of Model 1 can also be seen starting at the 128^{th} time step. At this moment, the aircraft has reached a quasi-steady-state and suddenly deflects the elevator. Model 1 uses the coefficient of drag due to elevator and angle of attack to predict the increase in drag and decrease in x force. Model 2 is less sensitive to this, as it also picks up drag perturbations from a subsequent aileron deflection. Notice that beyond that point, Model 1 x force follows a combination of the elevator deflection and angle of attack patterns while Model 2 x force is affected by the elevator deflection, angle of attack, and aileron deflection patterns.

- Third, it is apparent from Fig. 5.6 that the full aerodynamic model predicts much more moment about the z axis than the simplified equations. In fact, it predicts an order of magnitude difference in moment about the z axis. This could be related to the fact that the propeller model includes off-axis forces and moments caused by the propeller situated at an angle of incidence to the freestream velocity. In many situations, normal forces in the plane of the propeller rotation would cause a moment about the z axis.

Overall, both aerodynamic modeling results predict reasonable forces and moments. However, it is apparent by the complexity in the plotted results of the full aerodynamic model that this model is more sensitive and capable of modeling the full effects of various input perturbations not detected by the simplified equations model.

The autopilot code has been tested for its ability to control around the forces and moments predicted by the full aerodynamic model and found to be very successful during horizontal flight modes. The full aerodynamic model has not yet been employed during VTOL modes. This constitutes the remaining step for the full integration of the aerodynamic model into the 6 DOF simulator.

Chapter 6

Conclusion

6.1 Lifting Line Model

The lifting line algorithm has proven to be extremely fast and accurate for 3D wings below stall. This provides a very useful tool for the initial design stages of conventional aircraft. For wings above stall, the lifting line method can be used with caution. It has shown to produce reasonable values for the integrated lift on a wing. However, these solutions are often plagued with oscillations in the circulation distribution, which make the resulting lift, drag, and moment distributions hard to believe. Further investigation may be able to alleviate these drawbacks to convergence above stall. Additionally, it has been found that the lifting line theory has significant limitations in predicting 3D effects on a wing near 90° angle of attack. However, the results produced at high angles of attack are within reason, and can be used with caution.

6.2 Propeller Model

The accuracy of the propeller model is dependent upon the extent to which the propeller is correctly characterized within the model. When the propeller is correctly modeled, the propeller model appears to predict a slightly higher velocity profile than the experimental data. However, for the initial stages of VTOL aircraft design, the velocity profiles and slipstream geometry predicted by the model are acceptable. Thus, a method has been presented and validated which can quickly and accurately predict propeller slipstream characteristics. The speed of this solution along with its accuracy will allow the model to be used in preliminary design phases of a VTOL SUAV.

6.3 Combined Models

The results of the combined low-cost models presented above indicate that this overall approach shows promise for initial aerodynamic design calculations of wings with significant slipstream effects. The lifting line approach to modeling the wing aerodynamics produces satisfactory results in the presence of a slipstream, often to within the uncertainty of the experimental measurements. The propeller model also produces results in good agreement with experimental data. However, the combined wing and propeller models produce results that, although qualitatively correct, tend to over-predict the magnitude of the lift perturbations due to the slipstream. This behavior and its possible remedies should be further investigated.

6.4 Resulting Software: Aither

A software package for aircraft design resulted from the code described above. The code was written in C++ with a Graphical User Interface developed by Jeff Hogge. The software has proven to be user-friendly and will be implemented by aircraft design teams at Brigham Young University for future development of both conventional and VTOL aircraft.

Appendix A

Derivation of Lifting-Line Equation

A.1 Nomenclature

A_i area of wing section i

$\bar{c}_i$ characteristic chord length for wing section i

c_i average chord length at wing section i

C_{Di} section drag coefficient for wing section i

C_{Li} section lift coefficient for wing section i

$C_{L\alpha i}$ section lift slope for wing section i

C_{Mi} section moment coefficient for wing section i

$\mathbf{d\ell_i}$ directed differential vortex length vector at control point i

f system of equations

$\mathbf{F}$ total force on aircraft

$[\mathbf{J}]$ Jacobian matrix

$\mathbf{M}$ total moment on aircraft

N total number of horseshoe vortices

$\mathbf{R}$ residual vector

$\mathbf{r_i}$ vector from aircraft CG to control point i

$\mathbf{r_{i_1 j}}$ vector from 1^{st} node on section i to control point on section j

$\mathbf{r_{i_2 j}}$ vector from 2^{nd} node on section i to control point on section j

$r_{i_1 j}$ magnitude of $\mathbf{r_{i_1 j}}$

$r_{i_2 j}$ magnitude of $\mathbf{r_{i_2 j}}$

S_i planform area of wing section i

$\mathbf{u_{ai}}$ chordwise unit vector at control point i

$\mathbf{u_{ni}}$ normal unit vector at control point i

$\mathbf{u_{si}}$ spanwise unit vector at control point i

$\mathbf{u_i}$ unit vector in the direction of the local velocity

$\mathbf{v_{ij}}$ velocity induced at control point j by horseshoe vortex i

$\mathbf{V_{rel_i}}$ upstream velocity at control point i

$\mathbf{V_{tot_i}}$ total velocity at control point i

V_{tot_i} magnitude of $\mathbf{V_{tot_i}}$

α_i angle of attack at wing section i

δ_i flap deflection for wing section i

Γ_i vortex strength at control point i

ρ fluid density

A.2 Overview of Numerical Lifting Line Method

In the original numerical lifting line method, a finite wing is modeled using a series of horseshoe vortices with one edge bound to the quarter chord of the wing and the trailing portion aligned with the free-stream velocity. A general 3D vortex lifting law is combined with Prandtl's hypothesis that each spanwise section of the wing has a section lift equivalent to that acting on a similar 2D airfoil with the same local angle of attack.

From the 3D vortex lifting law, the differential force vector produced by the finite wing section i is

$$\mathbf{dF_i} = \rho\Gamma_i\mathbf{V_i} \times \mathbf{d}\ell_\mathbf{i} \tag{A.1}$$

The lift coefficient of a 2D airfoil can be expressed as an arbitrary function of angle of attack

$$C_{l_i} = C_{l_i}(\alpha_i, \delta_i) \tag{A.2}$$

Assuming that this relationship is known at each section, then the magnitude of the differential force produced by wing section i is

$$\mathbf{dF_i} = \frac{1}{2}\rho{\mathbf{V}_\infty}^2 C_{l_i}(\alpha_i, \delta_i)A_i \tag{A.3}$$

Setting the magnitude of Eq. (A.1) equal to the right hand side of Eq. (A.3) for each of the spanwise sections of the wing produces a system of equations that can be solved for the vortex strengths at each section. Once all the vortex strengths are known, the force vector at each section can be computed and summed together to determine the inviscid force and moment vectors acting on the wing. This method has been shown to work well at predicting the inviscid forces and moments for wings with sweep and dihedral and aspect ratios greater than 4. Accuracy is similar to panel methods or Euler computational fluid dynamics, but at a fraction of the cost. In addition, systems of lifting surfaces with arbitrary position and orientation can be analyzed.

A.3 Jacobian

Phillips [5] derives a nonlinear system of equations which can be solved for the vortex strengths at each section. This nondimensional approach works well for conventional aircraft where a freestream velocity can be used to nondimensionalize the flow. However, for VTOL flight analysis where the freestream velocity can approach zero, the nondimensional equations do not stand. The following derivation presents a similar result to Phillips's nondimensional derivation, but preserves the dimensional qualities of the flow and aircraft. Such an approach allows not only for freestream velocities to approach zero, but also for varying velocities across the wingspan.

We begin by setting the magnitude of the force obtained through the lift coefficient at wing section i equal to the magnitude of the forces obtained from the Γ values.

$$\rho\Gamma_i \left| \left(\mathbf{V_{rel_i}} + \sum_{j=1}^{N} \Gamma_j \mathbf{v_{ji}} \right) \times \mathbf{d\ell_i} \right| = \frac{1}{2}\rho V_{tot_i}^2 A_i Cl_i(\alpha_i, \delta_i) \tag{A.4}$$

where

$$\mathbf{v_{ij}} = \frac{1}{4\pi}\left[\delta_{ij}\frac{(r_{i_1 j}+r_{i_2 j})(\mathbf{r_{i_1 j}}\times\mathbf{r_{i_2 j}})}{r_{i_1 j}r_{i_2 j}(r_{i_1 j}r_{i_2 j}+\mathbf{r_{i_1 j}}\cdot\mathbf{r_{i_2 j}})}\right] + \frac{1}{4\pi}\left[\frac{\mathbf{u_\infty}\times\mathbf{r_{i_2 j}}}{r_{i_2 j}(r_{i_2 j}-\mathbf{u_\infty}\cdot\mathbf{r_{i_2 j}})} - \frac{\mathbf{u_\infty}\times\mathbf{r_{i_1 j}}}{r_{i_1 j}(r_{i_1 j}-\mathbf{u_\infty}\cdot\mathbf{r_{i_1 j}})}\right] \quad \text{(A.5)}$$

Rearranging and canceling ρ we get

$$2\Gamma_i\left|\left(\mathbf{V_{rel_i}}+\sum_{j=1}^{N}\Gamma_j\mathbf{v_{ji}}\right)\times\mathbf{d}\ell_\mathbf{i}\right| - V_{tot_i}^2 A_i Cl_i(\alpha_i,\delta_i) = 0 \quad \text{(A.6)}$$

The system of equations is then written in the vector form

$$F(\mathbf{\Gamma}) = \mathbf{R} \quad \text{(A.7)}$$

where

$$F_i(\mathbf{\Gamma}) = 2\Gamma_i\left|\left(\mathbf{V_{rel_i}}+\sum_{j=1}^{N}\Gamma_j\mathbf{v_{ji}}\right)\times\mathbf{d}\ell_\mathbf{i}\right| - V_{tot_i}^2 A_i Cl_i(\alpha_i,\delta_i) \quad \text{(A.8)}$$

We want to find the vector of vortex strengths $\mathbf{\Gamma}$ that makes the residual vector $\mathbf{R}$ approach zero. Therefore we want the change in the residual vector to be equal to $-\mathbf{R}$. If we start with an intial guess for the vector $\mathbf{\Gamma}$, we can use the Newton corrector equation and iterate until convergence criteria are met.

$$[\mathbf{J}]\mathbf{\Delta\Gamma} = -\mathbf{R} \quad \text{(A.9)}$$

where $[\mathbf{J}]$ is an N by N matrix of partial derivatives.

$$J_{ij} = \frac{\partial F_i}{\partial \Gamma_j} \quad \text{(A.10)}$$

Eq. A.10 takes on two different forms for two possible cases: Case 1: $i \neq j$ and Case 2: $i = j$. We will first look at Case 1.

Case 1: $\mathbf{i \neq j}$: $\frac{\partial F_i}{\partial \Gamma_j}$ can be divided into two parts (see Eq. (A.8). First, let's look at the derivative of the first half of the equation with respect to Γ_j:

$$\frac{\partial}{\partial \Gamma_j} 2\Gamma_i \left| \left(\mathbf{V_{rel_i}} + \sum_{j=1}^{N} \Gamma_j \mathbf{v_{ji}} \right) \times \mathbf{d\ell_i} \right| \tag{A.11}$$

This can be rewritten in generic notation as

$$\frac{\partial}{\partial t} |\mathbf{f} \times \mathbf{g}| = \frac{\mathbf{f} \times \mathbf{g}}{|\mathbf{f} \times \mathbf{g}|} \cdot \left(\frac{\partial \mathbf{f}}{\partial t} \times \mathbf{g} \right)$$

where $\mathbf{f}$ is a vector function of t and $\mathbf{g}$ is any vector that is not a function of t. Applying this rule to the equation yields:

$$\frac{\partial}{\partial \Gamma_j} 2\Gamma_i \left| \left(\mathbf{V_{rel_i}} + \sum_{j=1}^{N} \Gamma_j \mathbf{v_{ji}} \right) \times \mathbf{d\ell_i} \right| = \frac{2\mathbf{W_i} \cdot (\mathbf{v_{ji}} \times \mathbf{d\ell_i})}{|\mathbf{W_i}|} \Gamma_i \tag{A.12}$$

where

$$\mathbf{W_i} = \left(\mathbf{V_{rel_i}} + \sum_{j=1}^{N} \Gamma_j \mathbf{v_{ji}} \right) \times \mathbf{d\ell_i} \tag{A.13}$$

Now we turn our attention to the derivative of the second half of the equation with respect to Γ_j:

$$\frac{\partial}{\partial \Gamma_j} V_{tot_i}^2 A_i Cl_i(\alpha_i, \delta_i) \tag{A.14}$$

where

$$\mathbf{V_{tot_i}} = \mathbf{V_{rel_i}} + \sum_{j=1}^{N} \Gamma_j \mathbf{v_{ji}} \tag{A.15}$$

$$V_{tot_i} = |\mathbf{V_{tot_i}}| \tag{A.16}$$

and

$$\alpha_i = \tan^{-1} \left[\frac{\left(\mathbf{V_{rel_i}} + \sum_{j=1}^{N} \Gamma_j \mathbf{v_{ji}} \right) \cdot \mathbf{u_{ni}}}{\left(\mathbf{V_{rel_i}} + \sum_{j=1}^{N} \Gamma_j \mathbf{v_{ji}} \right) \cdot \mathbf{u_{ai}}} \right] \tag{A.17}$$

Here V_{tot_i} and Cl_i are both functions of Γ_j. The product rule is used for this part of the equation as follows:

$$\frac{\partial}{\partial t} f(t)g(t) = f'(t)g(t) + f(t)g'(t)$$

where $f(t)$ and $g(t)$ are both functions of t. Applying this rule to the equation yields:

$$\frac{\partial Cl_i}{\partial \alpha_i}\frac{\partial \alpha_i}{\partial \Gamma_j} V_{tot_i}^2 A_i + Cl_i(\alpha_i, \delta_i) A_i \frac{\partial}{\partial \Gamma_j}\left(|\mathbf{V_{tot_i}}|^2\right) \tag{A.18}$$

In order to solve for $\frac{\partial \alpha_i}{\partial \Gamma_j}$ we use the chain rule with the known derivatives of two basic equations:

$$\frac{\partial}{\partial u}\left(\tan^{-1} u\right) = \frac{1}{u^2+1}$$

$$\frac{\partial}{\partial u}\left(\frac{v}{u}\right) = \frac{v\partial u - u\partial v}{v^2}$$

Applying the chain rule and the above derivatives we get:

$$\frac{\partial \alpha_i}{\partial \Gamma_j} = \left[\frac{1}{\left(\frac{V_{ni}}{V_{ai}}\right)^2 + 1}\right]\left[\frac{V_{ai}(\mathbf{v_{ji}} \cdot \mathbf{u_{ni}}) - V_{ni}(\mathbf{v_{ji}} \cdot \mathbf{u_{ai}})}{V_{ai}^2}\right] \tag{A.19}$$

where

$$V_{ai} = \left(\mathbf{V_{rel_i}} + \sum_{j=1}^{N} \Gamma_j \mathbf{v_{ji}}\right) \cdot \mathbf{u_{ai}} \tag{A.20}$$

and

$$V_{ni} = \left(\mathbf{V_{rel_i}} + \sum_{j=1}^{N} \Gamma_j \mathbf{v_{ji}}\right) \cdot \mathbf{u_{ni}} \tag{A.21}$$

Simplifying yields

$$\frac{\partial \alpha_i}{\partial \Gamma_j} = \frac{V_{ai}(\mathbf{v_{ji}} \cdot \mathbf{u_{ni}}) - V_{ni}(\mathbf{v_{ji}} \cdot \mathbf{u_{ai}})}{V_{ai}^2 + V_{ni}^2} \tag{A.22}$$

Using rules of vector derivatives we find

$$\frac{\partial}{\partial \Gamma_j}\left(|\mathbf{V_{tot}}|^2\right) = 2(\mathbf{V_{tot}} \cdot \mathbf{v_{ji}}) \tag{A.23}$$

Substituting equations A.22 and A.23 into Eq. A.18 and then equations A.12 and A.18 into Eq. A.10, we get:

$$J_{ij} = \frac{\partial F_i}{\partial \Gamma_j} = \frac{2\mathbf{W_i} \cdot (\mathbf{v_{ji}} \times \mathbf{d}\ell_\mathbf{i})}{|\mathbf{W_i}|}\Gamma_i - V_{tot_i}^2 A_i \frac{\partial Cl_i}{\partial \alpha_i} \frac{V_{ai}(\mathbf{v_{ji}} \cdot \mathbf{u_{ni}}) - V_{ni}(\mathbf{v_{ji}} \cdot \mathbf{u_{ai}})}{V_{ai}^2 + V_{ni}^2} - 2A_i Cl_i(\alpha_i, \delta_i)(\mathbf{V_{tot}} \cdot \mathbf{v_{ji}}) \quad \text{(A.24)}$$

Case 2: $\mathbf{i = j}$: Now we turn to Case 2 where $i = j$. The derivation of Case 2 is identical to Case 1 except that an extra term appears in equation A.12 where $\Gamma_i = \Gamma_j$ which alters the derivative somewhat. Our new answer for Eq. A.12 is:

$$\frac{\partial}{\partial \Gamma_j} 2 \left| \Gamma_i \left(\mathbf{V_{rel_i}} + \sum_{j=1}^{N} \Gamma_j \mathbf{v_{ji}} \right) \times \mathbf{d}\ell_\mathbf{i} \right| = 2|\mathbf{W_i}| + \frac{2\mathbf{W_i} \cdot (\mathbf{v_{ji}} \times \mathbf{d}\ell_\mathbf{i})}{|\mathbf{W_i}|}\Gamma_i \quad \text{(A.25)}$$

As a result, we obtain

$$J_{ij} = \frac{\partial F_i}{\partial \Gamma_j} = 2|\mathbf{W_i}| + \frac{2\mathbf{W_i} \cdot (\mathbf{v_{ji}} \times \mathbf{d}\ell_\mathbf{i})}{|\mathbf{W_i}|}\Gamma_i - V_{tot_i}^2 A_i \frac{\partial Cl_i}{\partial \alpha_i} \frac{V_{ai}(\mathbf{v_{ji}} \cdot \mathbf{u_{ni}}) - V_{ni}(\mathbf{v_{ji}} \cdot \mathbf{u_{ai}})}{V_{ai}^2 + V_{ni}^2} - 2A_i Cl_i(\alpha_i, \delta_i)(\mathbf{V_{tot}} \cdot \mathbf{v_{ji}}) \quad \text{(A.26)}$$

J_{ij} can then be used in Eq. (15) to compute the correction vector $\mathbf{\Delta\Gamma}$. Using Newton's method, a new $\mathbf{\Gamma}$ vector is computed. This process is repeated until the residual vector, $\mathbf{R}$ reaches some convergence criteria.

A.4 Linear Approximation

In order to make the Newton iteration process converge as quickly as possible, it is important to obtain the best initial guess for the $\mathbf{\Gamma}$ vector as possible. To do this, a linear system of equations can first be solved. This system is constructed from the original system of equations by dropping all second order terms and using the small

angle approximation for the geometric and induced angles of attack. In the original system,

$$2\Gamma_i \left| \left(\mathbf{V_{rel_i}} + \sum_{j=1}^{N} \Gamma_j \mathbf{v_{ji}} \right) \times \mathbf{d\ell_i} \right| - V_{tot_i}^2 A_i C l_i(\alpha_i, \delta_i) = 0 \tag{A.27}$$

α_i is defined as

$$\alpha_i = \tan^{-1} \left[\frac{\left(\mathbf{V_{rel_i}} + \sum_{j=1}^{N} \Gamma_j \mathbf{v_{ji}} \right) \cdot \mathbf{u_{ni}}}{\left(\mathbf{V_{rel_i}} + \sum_{j=1}^{N} \ \Gamma_j \mathbf{v_{ji}} \right) \cdot \mathbf{u_{ai}}} \right] \tag{A.28}$$

Applying the small angle approximations,

$$\alpha_i = \left(\mathbf{V_{rel_i}} + \sum_{j=1}^{N} \Gamma_j \mathbf{v_{ji}} \right) \cdot \mathbf{u_{ni}} \tag{A.29}$$

Thus α_i can be approximated as the sum of the geometric angle of attack, α_{geom_i}, and the induced angle of attack, α_{ind_i}. Thus

$$\alpha_i = \alpha_{geom_i} + \alpha_{ind_i} \tag{A.30}$$

where

$$\alpha_{geom_i} = \frac{\mathbf{V_{rel_i}} \cdot \mathbf{u_{ni}}}{V_{rel_i}} \tag{A.31}$$

and

$$\alpha_{ind_i} = \sum_{j=1}^{N} \frac{\Gamma_j \mathbf{v_{ji}} \cdot \mathbf{u_{ni}}}{V_{rel_j}} \tag{A.32}$$

Here V_{rel_i} and V_{rel_j} are used to normalize the magnitudes of the dot products . Now α_i can be written as

$$\alpha_i = \left(\frac{\mathbf{V_{rel_i}} \cdot \mathbf{u_{ni}}}{V_{rel_i}} \right) + \left(\sum_{j=1}^{N} \frac{\Gamma_j \mathbf{v_{ji}} \cdot \mathbf{u_{ni}}}{V_{rel_j}} \right) \tag{A.33}$$

Additionally, we assume that the angle of attack is in the linear lift slope range. Thus,

$$C l_i(\alpha_i, \delta_i) = C_{L\alpha i} \left(\alpha_i - \alpha_{L0i} + \epsilon_i \delta_i \right) \tag{A.34}$$

By dropping all second order terms (substituting $\mathbf{V_{rel_i}}$ for $\mathbf{V_{tot_i}}$), the following equation is produced.

$$2\Gamma_i \left|\mathbf{V_{rel_i}} \times \mathbf{d\ell_i}\right| - V_{rel_i}^2 A_i C_{L\alpha i} \left[\left(\frac{\mathbf{V_{rel_i}} \cdot \mathbf{u_{ni}}}{V_{rel_i}}\right) + \left(\sum_{j=1}^{N} \frac{\Gamma_j \mathbf{v_{ji}} \cdot \mathbf{u_{ni}}}{V_{rel_j}}\right) - \alpha_{L0i} + \epsilon_i \delta_i\right] = 0 \tag{A.35}$$

A.35 can be rearranged to the linear system

$$\frac{2\Gamma_i}{A_i C_{L\alpha i}} \left|\mathbf{V_{rel_i}} \times \mathbf{d\ell_i}\right| - V_{rel_i}^2 \left(\sum_{j=1}^{N} \frac{\Gamma_j \mathbf{v_{ji}} \cdot \mathbf{u_{ni}}}{V_{rel_j}}\right) = V_{rel_i}^2 \left[\left(\frac{\mathbf{V_{rel_i}} \cdot \mathbf{u_{ni}}}{V_{rel_i}}\right) - \alpha_{L0i} + \epsilon_i \delta_i\right] \tag{A.36}$$

Once the resulting Γ vector is solved, it is used as the initial guess in the nonlinear system.

Bibliography

[1] P. Lotstedt, "Propeller slip-stream model in subsonic linearized potential flow," *Journal of Aircraft*, vol. 29, pp. 1098–1105, 1992. 3

[2] M. Metcalfe, "On the modelling of a fully-relaxed propeller slipstream," *AIAA/SAE/ASME/ASEE 21st Joint Propulsion Conference*, 1985. 3

[3] E. S. Levinsky, H. U. Thommen, P. M. Yager, and C. H. Holland, "Lifting-surface theory for V/STOL aircraft in transition and cruise. I," *Journal of Aircraft*, vol. 6, pp. 488–495, 1969. 3

[4] ——, "Lifting-surface theory for V/STOL aircraft in transition and cruise. II," *Journal of Aircraft*, vol. 7, pp. 58–65, 1970. 3

[5] W. Phillips and D. Snyder, "Modern adaptation of Prandtl's classic lifting-line theory," *Journal of Aircraft*, vol. 37, pp. 662–670, 2000. 4, 10, 12, 16, 33, 65

[6] R. H. Stone, "Aerodynamic modelling of a wing-in-slipstream tail-sitter UAV," *AIAA 2002 Biennial International Powered Lift Conference and Exhibit*, 2002. 4, 31

[7] B. W. McCormick, *Aerodynamics of V/STOL Flight*. New York: Academic Press, 1967. 4, 48, 49

[8] J. D. Anderson, *Fundamentals of Aerodynamics*, 3rd ed. Avenue of the Americas, New York, NY: McGraw-Hill, 2001. 9

[9] A. W. Winkelmann and J. B. Barlow, "A flowfield model for a rectangular planform wing beyond stall," *AIAA Journal*, vol. 18, pp. 1006–1008, 1980. 11

[10] J. D. Anderson, S. Corda, and D. M. V. Wie, "Numerical lifting line theory applied to drooped leading-edge wings below and above stall," *Journal of Aircraft*, vol. 17, pp. 898–904, 1980. 12, 16, 34, 36, 40

[11] W. F. Phillips, *Mechanics of Flight*. Hoboken, New Jersey: John Wiley & Sons Inc., 2004. 15, 16, 23, 24, 25, 30, 34, 55

[12] L. Prandtl and A. Betz, *Vier Abhandlungen zur Hydrodynamik und Aerodynamik*, Gottingen, 1927. 29, 30

[13] S. Goldstein, "On the vortex theory of screw propellers," *Royal Society of London Proceedings Series A*, vol. 123, pp. 440–465, April 1929. 29

[14] B. W. McCormick, *Aerodynamics, Aeronautics, and Flight Mechanics*. New York: John Wiley & Sons Inc., 1979. 31

[15] E. F. Weener, "Stalled and partially stalled high aspect ratio straight wings," *Ph.D. Dissertation, Dept. of Aerospace Engineering, Univ. of Michigan*, 1975. 34

[16] R. Mukherjee and A. Gopalarathnam, "Post-stall prediction of multiple-lifting-surface configurations using a decambering approach," *AIAA 2004-0219*, 2004. 34, 36

[17] W. R. Sears, "Some recent developments in airfoil theory," *Journal of Aeronautical Sciences*, vol. 23, pp. 490–499, 1956. 34

[18] A. Pope, "The forces and pressures over a NACA 0015 airfoil through 180 degrees angle of attack," *Georgia Tech. Rep.*, no. E-102, 1947. 39, 40

[19] C. C. Critzos, H. H. Heyson, and R. W. Boswinkel, "Aerodynamic characteristics of NACA 0012 airfoil section at angles of attack from 0° to 180°," *NACA TN-3361*, 1955. 40

[20] J. Stuper, "Effect of propeller slipstream on wing and tail," *NACA TM 874*, 1938. 41, 44, 45, 47, 52

[21] P. Spalart and S. Allmaras, "A one-equation turbulence model for aerodynamic flows," *AIAA Paper 92-0439*, 1992. 42

[22] M. A. Kotb and J. A. Schetz, "Measurement of three-dimensional turbulent flow behind a propeller in a shear flow," *AIAA Journal*, vol. 24, pp. 570–577, 1986. 47, 48, 49

[23] J. Lepicovsky and W. Bell, "Aerodynamic measurements about a rotating propeller with a laser velocimeter," *Journal of Aircraft*, vol. 21, pp. 264–271, 1984. 50, 51

[24] J. Nozieka, J. Novotny, and J. Maticha, "Research on the flow past an aircraft propeller," *Proceedings of PSFVIP-4*, 2003. 50, 51

[25] B. L. Stephens and F. L. Lewis, *Aircraft Control and Simulation*, 2nd ed. John Wiley & Sons Inc., 2004. 55

[26] N. B. Knoebel, S. R. Osborne, D. O. Snyder, T. W. McLain, R. W. Beard, and A. M. Eldredge, "Preliminary modeling, control, and trajectory design for miniature autonomous tailsitters," *Proceedings of the AIAA Guidance, Navigation, and Control Conference*, August 2006 Keystone, Colorado AIAA-2006-6713. 55